DIFFERENTIAL CONDUCTANCE OF A BALLISTIC QUANTUM WIRE IN THE PRESENCE OF RASHBA SPIN–ORBIT AND ZEEMAN INTERACTIONS

A thesis presented in partial
fulfilment of the requirements

for the degree

of Master of Philosophy

in Theoretical Condensed Matter Physics at
Massey University
New Zealand

Nitin Roy Nand
2007

Contents

Abstract

This thesis calculates the theoretical differential conductance of a ballistic quantum wire semiconductor nanostructure in the presence of Rashba spin–orbit and Zeeman interactions. In semiconductor heterostructures the Rashba spin–orbit interaction arises due to structure inversion asymmetry and couples the spin of the electron to its orbital momentum. In our work Zeeman interaction is induced by application of external magnetic fields in directions transverse, parallel, and perpendicular to the wire axis. Differential conductance is defined as the rate of change of current with respect to a voltage which is applied between two contacts, one on the left (source) and the other on the right (drain) side of the nanostructure.

The dispersion relations of the wire are obtained and from these differential conductance is calculated. Differential conductance is presented for zero and strong spin–orbit interaction situations and for magnetic fields applied in the various directions. The wire is studied under two specific regimes, namely normal and full Rashba mediated by the Rashba spin–orbit Hamiltonian. In the normal Rashba regime the wire is modelled without Rashba intersubband coupling while the full Rashba model includes this coupling.

Spin–orbit interaction and the direction of applied magnetic field significantly modifies dispersions and have drastic effects on the differential conductance profile. The application of magnetic field in directions parallel (and perpendicular) to the wire in the normal regime in the strong Rashba limit results in the formation of energy gaps. The presence of these gaps drastically reduces conductance. These gaps are suppressed in the full Rashba model of the wire in the strong Rashba limit and therefore reduction in conductance is not observed in the parallel and perpendicular field directions. In the normal Rashba regime in the strong Rashba limit conductance is enhanced for a greater range of source–drian bias voltages at low fields, especially for fields applied in the parallel (and perpendicular) directions. Whereas, in the full Rashba regime in the strong Rashba limit conductance is enhanced upto mid range fields and voltages for all field directions. In both Rashba regimes in the strong Rashba limit the overall conductance is reduced at low fields and voltages for all field directions. Hence, it is concluded that weak Zeeman and weak spin–orbit effects at low bias voltages favours electron transmission in ballistic quantum wires.

List of Figures

Acknowledgements

I thank the Institute of Fundamental Sciences (IFS)–Physics, College of Sciences, Massey University, Palmerston North, New Zealand for the opportunity to undertake the Master of Philosophy Degree in Theoretical Condensed Matter Physics. I sincerely thank my supervisor Dr. Ulrich Zülicke for identifying a suitable project for my thesis, his guidance and suggestions, sparing his time for me always, and his enlightening criticisms on the subsequent drafts. A special thank you goes to Dr. François Bissey of IFS–Physics for providing expertise on the LaTeX system for the preparation of this thesis. I also take this opportunity to dearly and heartfully thank my Mum and Dad for their moral and financial support, well wishes, and prayers.

....
Nitin Roy Nand
November, 2007.

Chapter 1

Introduction and Background

Over the past two decades the discovery of conductance quantisation in quantum point contacts and two–dimensional electron systems in a quantising magnetic field has initiated extensive research towards investigating transport properties in nanostructures related to the charge of the electron. In addition, the Coulomb blockade in quantum dots connected to conducting leads by high tunner barriers can be used to construct a single–electron transistor, in which switching between non–conducting and conducting states is done with a single charge [1, 2, 3]. Transport phenomenon in nanostructures that utilise the spin of the electron towards the understanding, designing, and implementation of novel spin–based electronic devices, however, have attracted considerable interest only during the past few years after the theoretical design of a spin–based transistor by Datta and Das in 1990 [4]. The field of spin electronics commonly known as spintronics includes the spin degree of freedom of an electron in addition to its charge and is a rapidly emerging, promising, and intriguing subject. Spintronics aims to bring novel functionalities to conventional electronic devices via the manipulation of electron spin by various means, such as imposing external electrical and magnetic fields to control and manipulate charge and spin dynamics. Although, advances have been made over the years in many areas including spin transport, spin dynamics, and spin relaxation, the full potential of spintronic applications in nanoscale electronic devices are yet to be developed and physically realised [5]. The cornerstone of the many advances in spintronics todate is the two–dimensional electron gas (Section 1.1).

Emerging research in the field of semiconductor nanoelectronics technology and mesoscopic physics have widely focused on the potential use of electron spin [3, 6]. The investigations encompass the broad field of spin–dependent quantum transport. One of which may involve studying ways in which electron spin can be effectively injected, manipulated, controlled, and detected across a semiconductor nanostructure and hybrid magnetic systems. Injecting electrons into a semiconductor from a ferromagnet is a standard way to generate spin–polarised current [7]. The giant magnetoresistance (GMR) effect, which was discovered in magnetic multilayers (consisting of an alternate stack of ferromagnetic and non–ferromagnetic metallic layers) finds applications in devices, such as GMR magnetic sensors and computer hard disk drive read heads for ultra high density magnetic recording [8]. Spin injection, manipulation, control, and detection are important

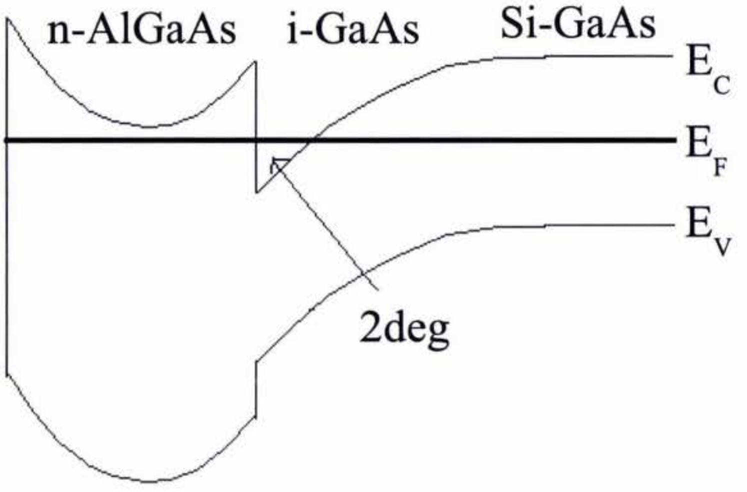

Figure 1.1: Schematic of the two–dimensional electron gas formed at the interface of n–AlGaAs/i–GaAs/Si–GaAs heterojunction by the bending of the conduction (E_C) and valence (E_V) energy bands. The Fermi level is shown by E_F. Adapted from [9].

considerations even in the design and development of novel futuristic spin–based electronic devices, such as spin–field effect transistors and circuits for spin–based quantum information processing [2].

1.1 The two–dimensional electron gas

The theoretical work reported in this thesis are based on GaAs–AlGaAs heterojunctions where a thin conducting layer is formed at the interface between GaAs and AlGaAs known as the two–dimensional electron gas (or 2deg in short). Since the Fermi energy of the wide gap AlGaAs layer is higher than that in the narrow gap GaAs layer, electrons spill over from AlGaAs (which is n–doped) leaving positively charged donors. This space–charge distribution gives rise to a triangular shaped electrostatic potential that causes the conduction and valence bands to bend as shown in Fig. 1.1. At equilibrium the Fermi energy is constant everywhere [10]. The advantages of using 2degs include mean free paths and coherence lengths that exceed tens of microns at low temperatures. These heterostructures have progressed tremendously since the early 1980s and provide the best realisation of a two–dimensional metal available today with very high electron mobilities corresponding to mean free paths larger than typical device dimensions [10, 11]. In these 2degs the electrons are confined along one direction, typically the perpendicular z axis, which is also the growth direction of the heterostructure, in the lowest quantum mechanical state at the GaAs/AlGaAs interface often referred to as a 2D quantum well. Thus, free–moving electrons with a renormalised effective mass $m = 0.067m_o$ (where m_o is the free electron mass) are only present in the remaining two dimensions (in–plane x and y) and are situated typically around 100 nm below the surface. The combination of intrinsic and silicon doped GaAs and n–AlGaAs semiconductor materials which have ideal properties, such as identical lattice constants (which minimises strain) and super clean growth conditions result in nearly defect free interfaces. Moreover, advanced modulation doping techniques removes the ionised Si–donor atoms away from the interface, which minimises scattering allowing the fabrication of extremely high mobility 2degs [10, 11, 12]. The practical importance of the 2deg lies in its use as field–effect transistors and are referred to as modulation doped field–effect (MODFET) or high electron mobility transistors (HEMT). Transistors built on these 2degs have the lowest noise, highest frequency responses, and superior power handling efficiencies and find extensive use in telecommunication applications. These electron gases even display integer [13] and fractional quantum Hall effects [14, 15, 16, 17] if cooled to low temperatures and placed in high magnetic fields.

The two–dimensional electron gas facilitates the study of low–dimensional physics in both theoretical and experimental aspects. The 2deg provides a platform where low–dimensional semiconductor devices can be experimentally realised by further nanostructuring the 2deg. The methods used can range from advanced lithography, molecular beam epitaxy, or ion beam implantation techniques [10, 11, 18, 19] to create mesoscopic devices of reduced dimensions, such as quantum wires, quantum point contacts, and quantum dots. Further limiting the motion of an electron in one or more spatial directions within the 2deg semiconductor heterostructure plane leads to quantum confinement. Quantum confinement gives rise to new and fundamentally important physics phenomenon, which otherwise is diminished in bulk 3D semiconductors and metals. It is therefore interesting to study quantum transport through these quantum confined mesoscopic systems. For a comprehensive review of quantum transport in semiconductor nanostructures and mesoscopic systems the reader is referred to Refs. [20, 21, 22].

1.2 Mesoscopic systems and ballistic quantum wires

Mesoscopic systems are of nanometric size as they lie in–between microscopic and macroscopic systems. Since mesoscopic systems are so small they rely on a completely quantum mechanical approach rather than a classical one to describe its electron transport properties, such as transmission and conductance. The most important parameters (or length scales) that describe mesoscopic systems are the phase coherence length ℓ_ϕ, Fermi wavelength λ_F, and the mean free path ℓ_e of electrons. In a mesoscopic device the ℓ_ϕ is much larger than the physical dimensions (length L and width W) of the device, while the λ_F is comparable to these dimensions. This means that the electron's wavefunction is coherent and the electron can physically "move" within the device as matter waves giving rise to interference effects. If ℓ_e is much larger than L and W the device is a *ballistic* one in which electrons propagate through the device without being scattered (either elastically or inelastically) due to impurities or phonons [23, 24, 25].

Ballistic quantum wires have been proposed as basic elements in the design of spin filters and spin transistors [26]. It is a central requirement to control and manipulate the spin of electrons with electric fields to realise such spintronic devices. In semiconductor heterostructures (2deg) the macroscopic electric field present along the z direction is a source of intrinsic spin–orbit effects [27, 28, 29, 30, 31]. These spin–orbit effects can be controlled and manipulated using split gates. Datta and Das [4] were first to describe how the electrical field of an external gate electrode could be used to manipulate the spin precession of a conduction electron. Crucial to this mechanism is the field–dependent spin–orbit interaction, which in narrow gap 2degs is modelled by the Rashba spin–orbit interaction (Rsoi) Hamiltonian (discussed in Chapter 2). The Rashba spin–orbit strength increases linearly with the electron wavevector [32]. Other authors, such as Nitta et al [33] and Grundler [34] have also demonstrated the tuning of the Rashba coupling by an external gate voltage and application of a back gate voltage in different semiconductors, respectively. Matsuyama et al [35] have also established the same in a p–type InAs semiconductor.

1.3 Past work on quantum wires

A vast range of literature is available which investigates various electronic transport properties in quantum wires and quasi–one dimensional electron systems (Q1Des). This thesis is focused on the electron transport properties of ballistic quantum wires with Rashba spin–orbit interactions and application of external magnetic fields. In this Section a few examples of work related to this thesis are presented highlighting the significant results. Studies on quantum wires with Rashba effect only are considered first followed by studies including magnetic fields.

1.3.1 Quantum wire with Rashba effect

Ando and Tamura [36] have investigated conductance fluctuations in quantum wires in the presence of strong Rashba effect but in the absence of a magnetic field. They reported that a strong spin–orbit interaction reduces the fluctuations by half. This result coincides with ours at zero bias voltages for a similar situation. The effect of the spin–orbit interaction arising via a lateral confinement potential and also from a perpendicular one (Rashba type) on the band structure and conductance of Q1Des were carried out by Moroz and Barnes [37]. They found that the spin–orbit contributions from these two different spatially directed potentials significantly affect the band structure by introducing a wavevector dependence to subband energies producing additional subband minima and inducing anticrossings between subbands. This observation is reported in this thesis at zero fields and strong Rashba spin–orbit effects as well.

Governale and Zülicke [38] presented analytical and numerical results for strong Rashba spin–orbit coupling on band structure, transport, and interaction effects in quantum wires. They found that for situations with only the lowest spin–split subbands occupied, the electrons close to the Fermi points of the same chirality can have approximately parallel spins. In another study of Rashba spin splitting in quantum wires conducted by Governale and Zülicke [39], they reported hybridisation of spin–split quantum wire subbands in cases of strong Rashba effect. They reported that hybridisation led to unusual spin structures, where the direction of motion of electrons can fix their spin states. This property is claimed to have important ramifications for linear transport in quantum wires giving rise to spin accumulation without magnetic fields or ferromagnetic contacts.

1.3.2 Quantum wire with Rashba effect and magnetic fields

Berggren et al [40] have studied the magnetoconductance of 1D subbands in a narrow 2deg in a GaAs/AlGaAs heterojunction and have reported magnetic field induced depopulation of the 1D subbands in the presence of a transverse magnetic field. A similar depopulation of 1D subbands was reported by Berggren et al [41] in narrow quasi–one dimensional quantum channels, this time by an application of a perpendicular field. In our study subband depopulation due to magnetic fields applied transverse, parallel, and perpendicular to the wire are reported consistently for both zero and strong spin–orbit situations. Zhao et al [42] have also reported magnetic depopulation of hybrid magneto-electric subbands in a quantum–well wire under application of an axial magnetic field.

Moroz and Barnes [43] have theoretically studied the effect of spin–orbit interaction on band structure and low temperature transport in long Q1Des in zero and weak magnetic fields applied perpendicular to the nanostructure. They reported that spin–orbit interaction has peculiar effects on the band structure. A study on antisymmetric spin filtering in Q1Des with uniform spin–orbit coupling and presence of a weak in–plane magnetic field was presented by Středa and Šeba [44]. They discovered the presence of an energy interval (a gap) in the electron energy spectrum at which the orientation of spin states is controlled by the direction of the electron velocity leading to the natural spin polarisation of the electron current, if the Fermi energy falls into this energy interval. The effect of spin–orbit interactions (without Rashba intersubband coupling) and in–plane magnetic fields on the conductance of a ballistic Q1Des was studied by Pershin et al [45]. They found that the interplay of the spin–orbit interaction with effective magnetic field significantly modifies the band structure producing additional subband extrema and energy gaps. Hence, introducing the dependence of the subband energies on the field direction. The presence of energy gaps are reported in this thesis for fields applied parallel (in–plane) and perpendicular to the wire axis for a similar model of the wire, as will be seen in Chapter 3. Serra et al [26] have analysed the spectral and transport properties of ballistic Q1Des in the presence of spin–orbit coupling and in–plane magnetic fields. Their results demonstrate that Rashba precession and intersubband coupling must be treated on equal footing for wavevectors near the magnetic–field–induced gaps. They found that intersubband coupling limits the occurrence of negative effective masses at the gap edges and modifies the linear conductance curves in the strong–coupling limit. Our study extends the work done by Serra et al [26] and Pershin et al [45] by including perpendicularly applied external magnetic fields and most significantly the application of a source–drain bias voltage to investigate its effect on the transport properties of a ballistic quantum wire.

Pereira and Miranda [46] investigated the effect of strong spin–orbit interaction on electronic transport through non–magnetic impurities in one–dimensional systems. When a perpendicular magnetic field is applied the electron spin polarisation becomes momentum dependent and spin–flip scattering appears to first order in the applied field, in addition to the usual potential scattering. They analysed a situation in which by tuning the Fermi level and the Rashba coupling the magnetic field can suppress the potential scattering. Debald and Kramer [47] investigated the influence of a perpendicular magnetic field on the spectral and spin properties of a ballistic Q1Des with Rashba effect. The magnetic field strongly alters the spin–orbit induced modification to the subband structure when the magnetic length becomes comparable to the lateral confinement. A subband–dependent energy splitting at $k = 0$ is found, which can be much larger than the Zeeman splitting attributed to the breaking of a combined spin orbital–parity symmetry. A similar subband energy splitting at $k = 0$ is also found in our work for perpendicularly applied fields in the absence of Rashba intersubband coupling.

Even though spin–orbit effects and magnetic field dependent electronic transport in quantum wires have been studied quite extensively in the past, a single investigation of the differential conductance of non–interacting electrons with source–drain bias voltage V_{sd} for both in–plane (transverse and parallel) and perpendicular magnetic fields with strong Rashba spin–orbit interaction has been lacking. The purpose of this thesis is to bridge this deficiency in the existing literature and contribute further to the existing knowledge in this field.

1.4 The purpose of this thesis

The process of electron transmission through quasi–one dimensional electron systems involves the redistribution of incoming electron fluxes amongst its discrete eigenenergy levels followed by adiabatic transport through them. The determination of the electron eigenenergies of a Q1Des is an integral part of solving a more general quantum transport problem. This is usually obtained via a numerical diagonalisation of an Hamiltonian that describes the motion of these electrons in the system. As this approach is particularly relevant to the ballistic transport regime [37, 48] similar to that investigated in our work, we use this same approach. Once the eigenenergies are known these are used to produce dispersion relations to deduce the band structure of the Q1Des. By varying a physical parameter, such as the source–drain bias voltage to probe the band structure the differential conductance can be calculated. This is the methodology used in our study to investigate the differential conductance of a ballistic quantum wire. Differential conductance $\triangle G$ is defined as the rate of change of current I with respect to the source–drain voltage V_{sd} (i.e., $\triangle G = dI/dV_{sd}$) and is discussed in Chapter 2.

The objective of this thesis is: i) to theoretically calculate the differential conductance of a ballistic quantum wire from the wire's electronic band structure (dispersion relations) in the presence of Rashba spin–orbit and Zeeman interactions, and ii) to investigate the interplay between the Rashba and Zeeman effects on the wire's differential conductance. This thesis shows how the differential conductance of a ballistic quantum wire varies with source–drain voltage, magnetic fields applied in various directions with respect to the wire axis, and with and without the Rashba spin–orbit interaction.

The organisation of this thesis is as follows: Chapter 2 discusses the theoretical aspects of the quantum wire investigated in this work and lays down the theoretical methodology; Chapter 3 presents the dispersions for the wire and discusses the interplay between the Rashba and Zeeman effects on the dispersions; the differential conductance results are presented and their features are discussed in Chapter 4 followed by a summary and conclusion of the study in Chapter 5.

Chapter 2

Theoretical Methodology

This Chapter is devoted to the theoretical aspects of the quantum wire investigated in this thesis. The model for the quantum wire with Rashba and Zeeman interaction is established and the Hamiltonians describing the motion of electrons in the wire are developed. The methods used to solve these Hamiltonians are explained as well. An elaboration on the application of the Landauer–Büttiker formalism in the derivation of the formula for calculating the differential conductance of the wire is also presented.

2.1 The quantum wire model

Based on the two–dimensional electron gas quantum well the general form of the physical Hamiltonian describing the quantum wire in our system reads

$$H_{qw} = H_o + V + H_{Rsoi} + H_z \tag{2.1}$$

where H_o is the quasi–free particle Hamiltonian of the lowest 2D subband in the 2deg for low enough electron densities and temperatures, V is the confinement potential, H_{Rsoi} represents the Rashba spin–orbit interaction (Rsoi), and H_z denotes the Zeeman interaction Hamiltonians. The quasi–free particle Hamiltonian H_o represents the kinetic motion of the electrons in the 2deg and is given by

$$H_o = \frac{p_y^2}{2m} + \frac{p_x^2}{2m} \tag{2.2}$$

where m denotes the effective electron mass. In order to study the coupling of a spin state (σ) and electron motion in real space (k) that arises due to spin–orbit interaction, the Hamiltonian (Eq. 2.2) requires correction.

2.1.1 The Rashba spin–orbit interaction

The quantum mechanical interaction between the orbital and spin degrees of freedom of an electron is referred to as the spin–orbit interaction (soi) or spin–orbit coupling (soc). The spin–orbit interaction couples the electron's spin with its orbital momentum. Although spin–orbit interaction is relativistic in nature, it can give rise to an observable modification of semiconductor band structure [37] (as seen in Chapter 3) and can have drastic effects on electron transport (Chapter 4). In semiconductor heterostructures due to the lack of structure symmetry, spin–orbit interaction is induced by macroscopic electric fields (assumed uniform) and directed along the z direction. Spin–orbit interaction of such type is known as the Rashba spin–orbit interaction. The study of the quantum wire in this thesis is focused on spin–orbit interactions of the Rashba type only. The other type of spin–orbit interaction is known as Dresselhaus [48, 49], which arises due to inversion asymmetry present in bulk semiconductor structures. The Hamiltonian that models the Rashba spin–orbit interaction is described by the expression [48, 50]

$$
\begin{aligned}
H_{Rsoi} &= \frac{\alpha_o}{\hbar}(\boldsymbol{\sigma} \times \mathbf{p})_z && (2.3)\\
&= i\alpha_o \left(\sigma_y \frac{\partial}{\partial x} - \sigma_x \frac{\partial}{\partial y} \right) && (2.4)\\
&= \frac{\alpha_o}{\hbar}(\sigma_x p_y - \sigma_y p_x) && (2.5)\\
&= \hbar\,\omega_x\,\alpha \begin{pmatrix} 0 & a \\ a^\dagger & 0 \end{pmatrix} && (2.6)
\end{aligned}
$$

where the dimensionless parameters

$$
\begin{aligned}
\alpha &= \alpha_o \sqrt{\frac{2m}{\hbar^3 \omega_x}}, && (2.7)\\
a &= \frac{p_y + i p_x}{\sqrt{2m\hbar\omega_x}}, \text{ and} && (2.8)\\
a^\dagger &= \frac{p_y - i p_x}{\sqrt{2m\hbar\omega_x}}. && (2.9)
\end{aligned}
$$

In Eq. 2.3 the sample dependent α_o characterises the effective Rashba spin–orbit strength of an electron propagating with momentum ($p = \hbar k$) and is proportional to the heterostructure interface electric field, $\mathbf{p}$ is the electron momentum operator, and $\boldsymbol{\sigma} = (\sigma_x, \sigma_y, \sigma_z)$ denotes the Pauli spin vector. The components of $\boldsymbol{\sigma}$ used to commonly describe the electron spin are given by the Pauli spin matrices (the generators for the $SU(2)$ group are proportional to these matrices)

$$
\sigma_x = \begin{pmatrix} 0 & 1 \\ 1 & 0 \end{pmatrix}, \sigma_y = \begin{pmatrix} 0 & -i \\ i & 0 \end{pmatrix}, \text{ and } \sigma_z = \begin{pmatrix} 1 & 0 \\ 0 & -1 \end{pmatrix}. \tag{2.10}
$$

In the absence of Rashba spin–orbit interaction the 2D subbands are degenerate as shown in Fig. 2.1 (a) for one subband. However, in the presence of Rashba spin–orbit interaction the spin degeneracy of the energy bands are lifted at $\mathbf{k} \neq 0$ and the split bands move in wavevector direction as shown in Fig. 2.1 (b). The total effective–mass Hamiltonian for a 2deg system with Rashba effect can be written as a 2×2 matrix

$$
H_{2D} = \begin{pmatrix} \frac{\hbar^2}{2m}(k_x^2 + k_y^2) & i\alpha k_x + \alpha k_y \\ -i\alpha k_x + \alpha k_y & \frac{\hbar^2}{2m}(k_x^2 + k_y^2) \end{pmatrix} \tag{2.11}
$$

where

$$H_{2D} = H_o + H_{Rsoi} \tag{2.12}$$

with H_o being the electronic kinetic energy part in the absence of the Rashba effect. The single–particle Schrödinger equation of the Hamiltonian H_{2D} describing the 2D electronic motion can be straightforwardly solved to produce eigenenergy states of the form

$$E(k) = \frac{\hbar^2 k^2}{2m} \pm \alpha k, \tag{2.13}$$

which result in the two separate spin–split states as shown in Fig. 2.1 (b). The electronic eigenstates are labeled by a 2D wavevector $\vec{k}$ and the quantum number $\sigma = \pm 1$ of spin projection in the direction perpendicular to both $\vec{k}$ and the growth direction. The energy eigenvalues for states having the same $k = \|\vec{k}\|$ but opposite σ turns out to differ by a zero–field spin splitting energy $\Delta E_k = \pm\alpha k$. As time–reversal symmetry is preserved by the Hamiltonian H_{2D}, Rashba spin splitting does not result in a finite global magnetisation of the 2D electron system and no common spin quantisation axis can be found for its eigenstates [39]. The presence of a magnetic field induces Zeeman spin splitting (Zss) and the subbands split differently.

2.1.2 The Zeeman interaction

The Zeeman interaction couples electron spin to a applied magnetic field. In this study Zeeman interaction is induced by application of external magnetic fields in three independent spatial directions, transverse (x), parallel (y), and perpendicular (z) to the wire as shown in the schematic for the quantum wire (Fig. 2.2). The application of this external magnetic field does not introduce a vector potential dependence in our wire Hamiltonian model. The Zeeman interaction is represented by the Hamiltonian

$$H_z = \frac{1}{2} g \mu_B \boldsymbol{\sigma} \cdot \mathbf{B} \tag{2.14}$$

where g is the electron Landé factor, μ_B the electron Bohr magneton, $\boldsymbol{\sigma}$ denotes the Pauli spin vector, and $\mathbf{B}$ is the magnetic field vector. When only the magnetic field is present (i.e., Zss only) the subbands split and move vertically in energy direction for all values of $\mathbf{k}$ as depicted in Fig. 2.1 (c). As the magnetic field strength increases the Zeeman energy spacing between the split states becomes large. In the transport model of the wire the magnetic field applied at each direction is represented as a ratio relative to a typical magnetic field parameter B_o. In GaAs nanostructures B_o of a few Teslas yield magnetic lengths of a few tens of nm for wire widths of a few 100 nm. The source–drain voltage V_{sd} appears in the transport model through $V = V_{sd}/V_o$ where V_o represents the inherent voltages (in the order of a few Volts) due to electric fields in the 2deg.

In our work the quantum wire is modelled via a lateral electrostatic parabolic oscillator confinement potential in the transverse (x) direction given by

$$V(x) = \frac{1}{2} m \omega_x^2 x^2 \tag{2.15}$$

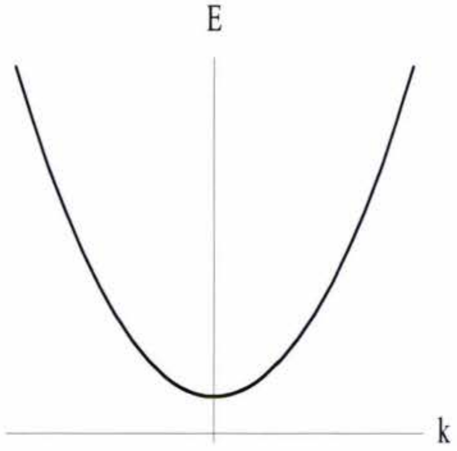

(a) Zero Rashba, zero Zeeman splitting

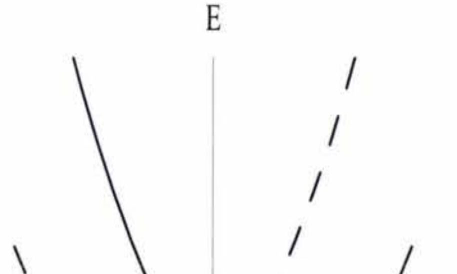

(b) Strong Rashba splitting

(c) Strong Zeeman splitting

Figure 2.1: Schematic dispersions showing splitting for one subband only. (a) Zero Rashba and Zeeman spin splitting, (b) due to strong Rashba splitting at zero magnetic field, and (c) in the presence of a strong magnetic field only (Zss). The solid and broken curves represent the spin–split states.

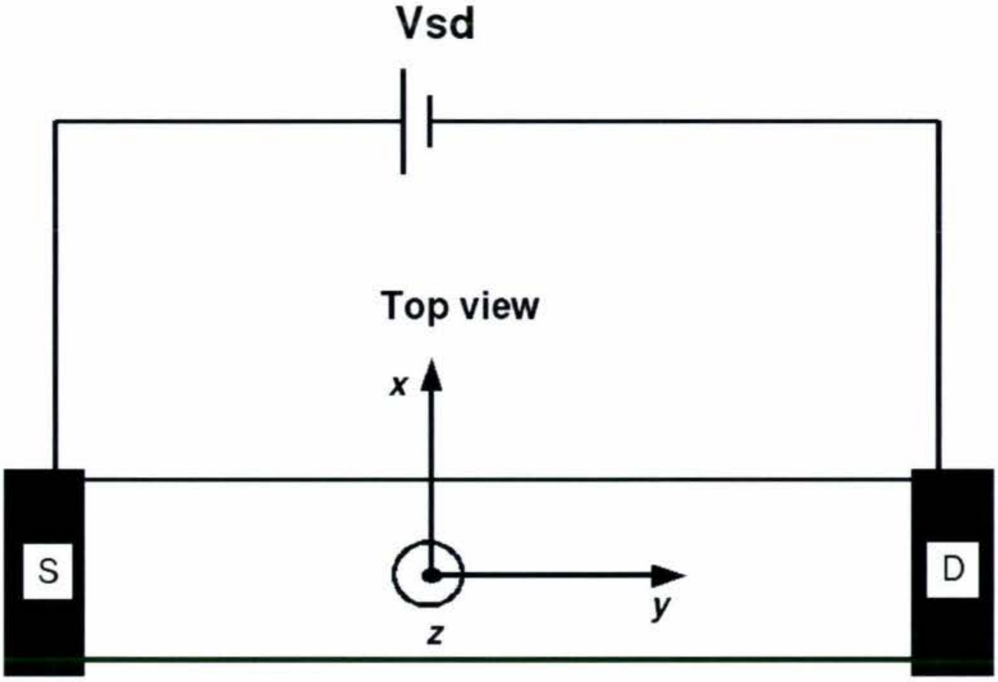

Figure 2.2: Schematic of the quantum wire studied in this thesis showing the coordinate system and the source (S) and drain (D) contacts.

where ω_x characterises the oscillator frequency. This potential further confines electrons in the x direction leaving *free* electron propagation in the wire direction y only, creating a quasi–one dimensional electron system. In the absence of spin–orbit interaction the single–electron spectrum is composed of quasi–1D subbands having quadratic dispersions in the 1D wavevector k_y that label its eigenstates. The characteristic energy scale for subband bottoms is related to the width of the quantum wire. For finite α the energy eigenstates are still plane waves in wire direction y, but the linear dependence of H_{Rsoi} on the momentum p_x in the confinement direction introduces a coupling between the quasi–1D subbands [39].

2.2 The normal and full Rashba regimes

The full physical single–electron Hamiltonian H_{qw} for the quantum wire in the effective–mass approximation is thus given by

$$H_{qw} = \frac{p_y^2}{2m} + \frac{p_x^2}{2m} + \frac{1}{2}m\omega_x^2 x^2 + \frac{\alpha}{\hbar}(\sigma_x p_y - \sigma_y p_x) + \frac{1}{2}g\mu_B\,\boldsymbol{\sigma}\cdot\mathbf{B}. \tag{2.16}$$

Based on the full Rashba spin–orbit interaction Hamiltonian H_{Rsoi} (Eq. 2.3) two regimes to study the quantum wire are identified, characterised by the two components of the Rashba Hamiltonian. In the first regime (hereafter referred to as normal Rashba) only the component that commutes with the momentum in the wire direction (y) with spin in the

x, that is

$$H_{norm} = \frac{\alpha}{\hbar}\sigma_x p_y \tag{2.17}$$

is incorporated in the wire Hamiltonian. The inclusion of the other component, that is

$$H_{mix} = -\frac{\alpha}{\hbar}\sigma_y p_x \tag{2.18}$$

forms the second regime (hereafter referred to as full Rashba). This term (Eq. 2.18) induces "mixing" between adjacent subbands with opposite spins, a phenomenon referred to as the Rashba intersubband coupling (Ric). The Rashba intersubband coupling has significant effects on dispersions (seen in Chapter 3) and hence differential conductance (Chapter 4). With this distinction the respective physical forms of the quantum wire Hamiltonian models representing the wire in the normal and full Rashba regimes are given by

$$H_{qwnRas} = \frac{p_x^2}{2m} + \frac{1}{2}m\omega_x^2 x^2 + \frac{\hbar^2 k_y^2}{2m} + \frac{\hbar^2 k_y k_{so}\sigma_x}{m} + \frac{1}{2}g\mu_B(\sigma_x B_x + \sigma_y B_y + \sigma_z B_z) \text{ and} \tag{2.19}$$

$$H_{qwfRas} = \frac{p_x^2}{2m} + \frac{1}{2}m\omega_x^2 x^2 + \frac{\hbar^2 k_y^2}{2m} + \frac{\hbar^2 k_y k_{so}\sigma_x}{m} - \frac{\alpha}{\hbar}\sigma_y p_x + \frac{1}{2}g\mu_B(\sigma_x B_x + \sigma_y B_y + \sigma_z B_z) \tag{2.20}$$

where $k_{so} = m\alpha/\hbar^2$ is the Rashba wavevector. Using the 1D plane–wave representation we can re–write the full Rashba quantum wire Hamiltonian (Eq. 2.20) in the form

$$H_{qwfras} = H_{sb} + H_{1D} + H_{mix} + H_z \tag{2.21}$$

where

$$H_{sb} = \frac{p_x^2}{2m} + \frac{1}{2}m\omega_x^2 x^2, \tag{2.22}$$

$$H_{1D} = \frac{\hbar^2 k_y^2}{2m} + \frac{\hbar^2 k_y k_{so}\sigma_x}{m}, \text{ and} \tag{2.23}$$

$$H_z = \frac{1}{2}g\mu_B(\sigma_x B_x + \sigma_y B_y + \sigma_z B_z). \tag{2.24}$$

The eigenenergy levels of H_{sd} are well known and represent the energy levels ($n = 0, 1, 2, ...$) of an harmonic oscillator

$$E_{sb} = \hbar\omega_x\left(n + \frac{1}{2}\right). \tag{2.25}$$

A length scale $k_{so}l_\omega$ where

$$l_\omega = \sqrt{\frac{\hbar}{m\omega_x}} \tag{2.26}$$

is the oscillator length (which corresponds to the width of the wire) is used to model the wire for zero and strong Rashba spin splitting (Rss) scenarios. As the spin precession length is given by

$$l_{so} = \frac{\pi}{k_{so}}, \tag{2.27}$$

$k_{so}l_\omega \rightarrow 1$ means that the wire width and the spin precession length are comparable. In this case the characteristic energy spacing between the subbands $\hbar\omega_x$ is comparable to the Rashba energy scale

$$\Delta_{so} = \frac{\hbar^2 k_{so}^2}{2m} \tag{2.28}$$

defining a situation in the strong Rashba limit with strong Rashba spin splitting. When $k_{so}l_\omega \rightarrow 0$ the subband spacing is large compared to the Rashba energy scale defining a situation in the zero Rashba limit with very small (or zero) Rashba spin splitting.

Since the wire Hamiltonians for both Rashba regimes are solved for each magnetic field direction, only the component in the Zeeman term (H_z) that corresponds to this field direction are taken into consideration in the calculations. A total of four energy levels (i.e., four subbands) are studied in this work and considered enough to adequately represent the relevant wire characteristics. Since each subband is spin–split an 8×8 eigenvalue Hamiltonian problem is solved in this work to obtain the spin resolved eigenenergy levels for the quantum wire in the two Rashba regimes, magnetic field directions (x, y, and z), and at zero and strong Rashba spin splitting scenarios. The actual physical forms of these Hamiltonians for each magnetic field direction and their respective eigenenergy expressions are contained in Appendix A.

2.3 Solving an eigenvalue Hamiltonian problem

The methods for solving an eigenvalue problem in quantum mechanics is standard, are well established and can be found in many quantum mechanics texts and other publications, for example Refs. [23, 25, 48, 51, 52, 53, 54]. An eigenvalue problem is generally represented by

$$H\Psi = E\Psi \tag{2.29}$$

where one solves the Shrödinger equation to deduce the real eigenenergy levels E through an Hermitian Hamiltonian H (usually in matrix form) in the basis of the eigenfunctions given by Ψ. The eigenvalues are determined by solving the characteristic polynomial of H (by setting the determinant to zero)

$$det(H - EI) = 0 \tag{2.30}$$

where I represents the identity matrix. Because of the translational invariance in the longitudinal (y) direction of the wire the eigenfunctions can be decomposed into a plane wave $e^{ik_y y}$ in the longitudinal direction and a spinor $\phi_n(x)$, which depends only on the transversal (x) direction such that

$$\Psi_n(x, y) = e^{ik_y y}\phi_n(x). \tag{2.31}$$

With the eigenfunctions defined as in Eq. 2.31 and the bosonic operators defining the number operator $\hat{n}_n$ such that

$$\hat{n}_n = a_n^\dagger a_n \tag{2.32}$$

where $a_n^\dagger$ (a_n) raises (lowers) a subband index for fixed n for a shifted harmonic oscillator describing the energy levels of the quasi–1D subbands (in the case without spin–orbit interaction), the transversal wavefunction component satisfies the equation

$$H(n)\phi_n(x) = E_n\phi_n(x). \tag{2.33}$$

In our work the eigenenergy levels for the quantum wire are obtained by first converting the physical Hamiltonians into their respective matrix forms and then diagonalising the matrix Hamiltonians using software–based numerical (perturbative) techniques. As the value of the Rashba interaction strength characterising a scenario for strong Rashba spin splitting does not exceed 1 ($k_{so}l_\omega = 0.9$), degenerate perturbation theory is employed to seek solutions of the perturbed states (due to H_{mix}) in terms of the known unperturbed states $|n,\sigma\rangle$. The unperturbed spin degenerate states have the form $|n,\sigma\rangle \rightarrow e^{ik_yy}\phi_n(x)|\sigma\rangle$ where $\sigma =\uparrow,\downarrow$ with the definitions of the spinors $|\uparrow\rangle = \binom{1}{0}$ and $|\downarrow\rangle = \binom{0}{1}$. Thus, the total matrix Hamiltonians are spanned in the basis of energy and spin and the matrix elements are given by

$$\langle n,m|H|\sigma,\sigma^{'}\rangle, \tag{2.34}$$

while the matrix elements of H_{mix} are obtained via

$$\langle n,\sigma|H_{mix}|m,\sigma^{'}\rangle = \langle n|p|m\rangle \otimes \langle\sigma|s|\sigma^{'}\rangle \tag{2.35}$$

where p and s represents the momentum and spin operators, respectively.

The methods used in our work is standard for solving any eigenvalue problem in quantum mechanics. Other authors, such as Serra et al [26], Pershin et al [45], Debald and Kramer [47], Mireles and Kirczenow [50], and Knobbe and Schäpers [55] have also used a similar approach in their investigations of the quantum wire. The 8×8 matrix representations of the total Hamiltonian describing the quantum wire in the normal and full Rashba regimes are contained in Appendix B together with examples of the resulting Hamiltonian matrices and their respective eigenenergy levels in different Rashba spin splitting situations for field applied in the transverse (x) direction.

Once the energy levels are obtained dispersion relations are plotted. The eigenenergy expressions are plotted as a function of another length scale k_yl_w, which corresponds to the propagating wavevector in direction y. From the dispersions the differential conductance of the wire are calculated.

2.4 The derivation of the differential conductance formula

In this Section the formula for the differential conductance (ΔG) is derived. The derivation of ΔG is based on the Landauer–Büttiker formalism described elsewhere, for example Datta [10], and Ferry and Goodnick [11]. The quantum wire is modelled such that it lies between two electron reservoirs. An electron incident from the source lead (left) with an energy E has a transmission probability $T(E)$ to travel through the wire into the drain lead (right). By determining $T(E)$ for a range of energies around the Fermi energy E_F of the source lead, the finite temperature, finite source–drain voltage V_{sd}, and Landauer formula can be used to calculate the transmitted current I as a function of the source–drain bias voltage (which is applied between the source and drain leads, see Fig. 2.2). The transmitted current formula as a function of V_{sd} [10, 45, 56, 57] is given by

$$I(V_{sd}) = \frac{2e}{h}\int_{-\infty}^{+\infty} T(E)(f_s(E,V_{sd}) - f_d(E,V_{sd}))dE \tag{2.36}$$

where $f_s(E,V_{sd})$ and $f_d(E,V_{sd})$ are the Fermi distribution functions of the electrons in the source and drain leads, respectively, in terms of energies E of the electrons and V_{sd}. The Fermi functions are given by

$$f_s(E,V_{sd}) = \frac{1}{1+\exp\left(\frac{E-\mu_s}{kT}\right)} = \frac{1}{1+\exp\left(\frac{E-E_F-\frac{eV_{sd}}{2}}{kT}\right)} \text{ and} \tag{2.37}$$

$$f_d(E,V_{sd}) = \frac{1}{1+\exp\left(\frac{E-\mu_d}{kT}\right)} = \frac{1}{1+\exp\left(\frac{E-E_F+\frac{eV_{sd}}{2}}{kT}\right)} \tag{2.38}$$

where

$$\begin{aligned} \mu_s &= E_F + \frac{eV_{sd}}{2} \text{ and} \\ \mu_d &= E_F - \frac{eV_{sd}}{2} \end{aligned} \tag{2.39}$$

represents the electrochemical potentials of the electrons in the source and drain, k is the Boltzmann constant, and T is the temperature.

Since differential conductance is defined as the derivative of the current with respect to voltage, we have

$$\frac{dI(V_{sd})}{dV_{sd}} = \Delta G = \frac{2e}{h}\int_{-\infty}^{+\infty} T(E)\left(\frac{\partial f_d(E,V_{sd})}{\partial V_{sd}} - \frac{\partial f_s(E,V_{sd})}{\partial V_{sd}}\right)dE. \tag{2.40}$$

Since

$$\frac{\partial f_d(E,V_{sd})}{\partial V_{sd}} = \frac{e}{2}\frac{\partial f_d(E,V_{sd})}{\partial E} \text{ and} \tag{2.41}$$

$$\frac{\partial f_s(E,V_{sd})}{\partial V_{sd}} = -\frac{e}{2}\frac{\partial f_s(E,V_{sd})}{\partial E}, \tag{2.42}$$

Eq. 2.40 becomes

$$\Delta G = \frac{2e}{h}\int_{-\infty}^{+\infty} T(E)\left(\frac{\partial f_d(E,V_{sd})}{\partial E} - \frac{\partial f_s(E,V_{sd})}{\partial E}\right)dE. \tag{2.43}$$

Moreover, at $T = 0K$ the partial differentials of the Fermi function with respect to energy in Eq. 2.43 can be approximated as delta functions such that

$$\frac{\partial f_d(E, V_{sd})}{\partial E} \approx \delta(E_F - E) = \delta\left(E_F - \frac{eV_{sd}}{2}\right) \text{ and} \tag{2.44}$$

$$\frac{\partial f_s(E, V_{sd})}{\partial E} \approx \delta(E_F - E) = \delta\left(E_F + \frac{eV_{sd}}{2}\right). \tag{2.45}$$

Since

$$T(E) = \sum M(E) \tag{2.46}$$

$$= \sum_n \theta(E - E_n) \tag{2.47}$$

where

$$M(E) = \theta(E - E_n) \tag{2.48}$$

is the number of subbands present below E, and E_n is the nth energy level of the 1D subbands, Eq. 2.43 becomes

$$\Delta G = \frac{e}{h}\sum_n \int_{-\infty}^{+\infty} \theta(E - E_n)\left(\delta\left(E_F - \frac{eV_{sd}}{2} - E\right) + \delta\left(E_F + \frac{eV_{sd}}{2} - E\right)\right). \tag{2.49}$$

Equation 2.49 further simplifies to

$$\Delta G = \frac{e}{h}\sum_n \theta\left(E_F - \frac{eV_{sd}}{2} - E_n\right) + \theta\left(E_F + \frac{eV_{sd}}{2} - E_n\right) \tag{2.50}$$

by applying the fundamental property of delta functions

$$\int_{-\infty}^{+\infty} f(x)\delta(x - a) = f(a). \tag{2.51}$$

The differential conductance of the wire is calculated via Eq. 2.50. The differential conductance formula compares the subband energies with changes in the electrochemical potentials of the left and right electron reservoirs as V_{sd} is varied. This is further explained in Chapter 4.

Chapter 3

Dispersions

This Chapter presents the dispersion relations for the quantum wire. As the dispersions for the wire arising in the normal Rashba model changes only gradually with magnetic field for each field direction, only a few specific dispersion plots to illustrate this are shown. Complete evolution of the dispersions are shown for the full Rashba model as significant changes are observed with increasing magnetic fields applied in the transverse (x), parallel (y), and perpendicular (z) directions. The dispersions are shown only for the strong Rashba limit (i.e., $k_{so}l_{\omega} = 0.9$). The magnetic field is varied in the range 0 to 0.9 relative to B_o. The dispersions pertaining to the normal Rashba model are presented in Section 3.1 followed by those for full Rashba in Section 3.2. The subbands are colour coded with the first being red, second blue, third green, and fourth magneta. Solid curves represent one spin state while broken curves the other.

3.1 Normal Rashba dispersions

Since the normal Rashba wire model does not incorporate Rashba intersubband coupling the dispersion curves arising for this model are void of non–parabolicities due to spin textures. However, non–parabolicities arising from energy gaps and band maxima are present. At zero magnetic field the dispersions are identical. The dispersions obtained for fields applied in the y and z directions are identical as well. Therefore, Fig. 3.1 only shows the dispersions corresponding to zero and maximum magnetic field values for field applied in the transverse (x) direction and for maximum field in the parallel (y) direction. In Fig. 3.1 plot (c) clearly shows the non–parabolicities that arises due to energy gaps when magnetic field is applied in the y (and z) directions. The dispersions which exhibit non–parabolicities due to the Rashba intersubband coupling are presented in Section 3.2.

3.1.1 Transverse (x) magnetic field

The eigenenergy expression that governs the dispersions for magnetic field applied in the x direction reads

$$\frac{2E_{n,k,\sigma}}{\hbar\omega_x} = 2n + 1 \pm B_x \pm 2(k_{so}l_{\omega})(k_y l_{\omega}) + (k_y l_{\omega})^2 \tag{3.1}$$

where n marks the subband index and B_x is the magnetic field in the x direction. At $k_{so}l_\omega = 0.9$ and $B_x = 0$ the eigen expression (Eq. 3.1) reduces to

$$\frac{2E_{n,k,\sigma}}{\hbar\omega_x} = 2n + 1 \pm 1.8(k_y l_\omega) + (k_y l_\omega)^2, \tag{3.2}$$

which represents subbands that are significantly spin–split in the wavevector direction (k_y) due to a strong contribution from the Rashba spin–orbit interaction (see plot (a) in Fig. 3.1). As the field increases the spin–split subbands shift in energy direction due to the increasing Zeeman effect. The subband bottom energy separation also increases with the field. The dispersion plot (b) in Fig. 3.1 describes a situation when the Rashba and Zeeman spin splittings are comparable as $k_{so}l_\omega = B_x = 0.9$. The eigen expression corresponding to plot (b) is

$$\frac{2E_{n,k,\sigma}}{\hbar\omega_x} = 2n + 1 \pm 0.9 \pm 1.8(k_y l_\omega) + (k_y l_\omega)^2. \tag{3.3}$$

Dispersion curves showing similar features have been obtained by Serra et al [26] and Pershin et al [45] in the strong Rashba limit (but without Ric) and Zeeman effects induced by in–plane (transverse) magnetic fields.

3.1.2 Parallel (y) and perpendicular (z) magnetic field

The eigenenergy expression that governs the dispersions for magnetic fields applied in the y and z are exactly the same and have the analytical form

$$\frac{2E_{n,k,\sigma}}{\hbar\omega_x} = 2n + 1 + (k_y l_\omega)^2 \pm \sqrt{B_{y,z}^2 + 4(k_{so}l_\omega)^2(k_y l_\omega)^2}. \tag{3.4}$$

At $k_{so}l_\omega = 0.9$ and $B_{y,z} = 0$ Eq. 3.4 reduces to

$$\frac{2E_{n,k,\sigma}}{\hbar\omega_x} = 2n + 1 + (k_y l_\omega)^2 \pm \sqrt{3.24(k_y l_\omega)^2}, \tag{3.5}$$

which is equivalent to Eq. 3.2 and represents subbands that are already split in the wavevector direction as shown in plot (a). However, as the field (Zeeman) increases a gap opens between the split subbands (around $k_y = 0$) and continues to widen as the field increases. The resulting dispersion plot (c) shows this feature at $B_{y,z} = 0.9$ and have an eigenenergy expression

$$\frac{2E_{n,k,\sigma}}{\hbar\omega_x} = 2n + 1 + (k_y l_\omega)^2 \pm \sqrt{0.81 + 3.24(k_y l_\omega)^2}. \tag{3.6}$$

These results demonstrate lifting of spin degeneracy around $k_y = 0$ due to application of in–plane (parallel) magnetic fields and supports the findings which have been reported by Serra et al [26] and Pershin et al [45] in their works. Our study shows that applying magnetic fields in the perpendicular direction also lifts spin degeneracy around $k_y = 0$. Thus, our results confirm that application of magnetic fields parallel and perpendicular

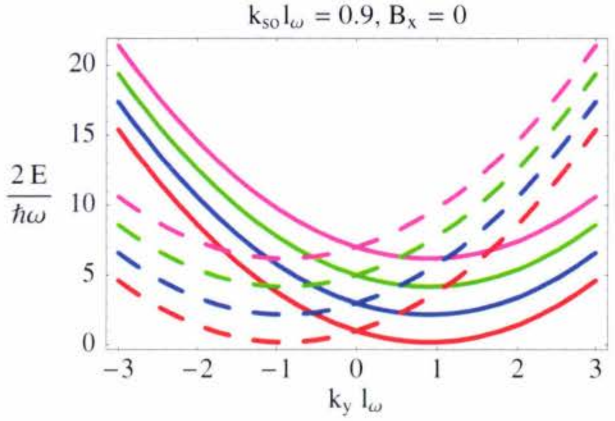

$k_{so} l_\omega = 0.9, B_x = 0$

(a) Transverse (x), zero field

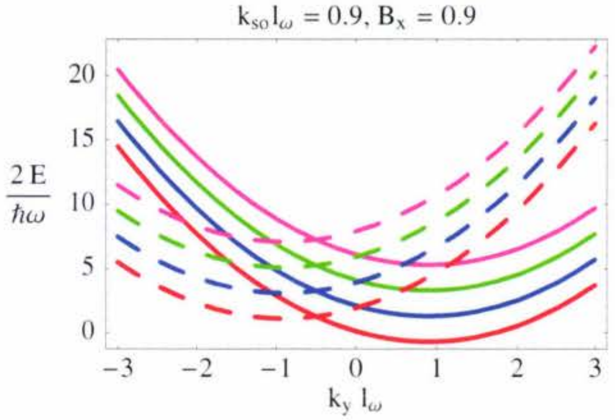

$k_{so} l_\omega = 0.9, B_x = 0.9$

(b) Transverse (x), maximum field

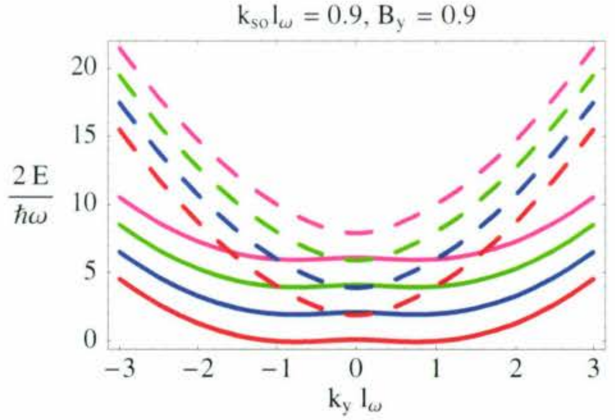

$k_{so} l_\omega = 0.9, B_y = 0.9$

(c) Parallel (y), maximum field

Figure 3.1: Dispersions for strong Rss corresponding to (a) zero and (b) maximum magnetic fields applied in the transverse (x), and (c) for maximum magnetic fields applied in the parallel (y) directions in the normal Rashba wire model.

to the wire in the strong Rashba limit, but without Rashba intersubband coupling gives rise to non–parabolicities in the band structure by forming energy gaps (or band maxima) around $k_y = 0$. In the dispersions seen in Figs. 3.3 and 3.4 for the full Rashba model of the wire (which incorporates Ric) the formation of these gaps around $k_y = 0$ are significantly diminished. This reduction in energy gaps suggests that Rashba intersubband coupling hinders the formation of band maxima, thereby restoring spin degeneracy in accordance to the findings reported by Serra et al [26]. The band maxima around $k_y = 0$ has been stated to have serious implications on electron transport as it reduces conductance and must be subtracted [26] to yield the correct differential conductance. This correction has been made in our calculations and shows startling results (see Chapter 4).

3.2 Full Rashba dispersions

The dispersions pertaining to the full Rashba model of the wire which includes Rashba intersubband coupling are presented in this Section.

3.2.1 Transverse (x) magnetic field

Figure 3.2 shows the evolution of dispersions for strong Rss in the full Rashba regime and for magnetic field applied in the x direction. Due to the Rashba intersubband coupling the dispersions are non–parabolic even at zero magnetic field — especially noticeable in the first three spin–split subbands (plot (a) in Fig. 3.2). This case has been studied in detail by Governale and Zülicke [38]. The mixing component of the full Rashba Hamiltonian is known to couple adjacent subbands with opposite spins giving rise to such spin textures (or anticrossings). In this case no common spin quantisation axis can be defined for eigenstates within any subband [39]. In these plots the effect is noticeable for the second and third split subbands (notice how close the blue dashed (solid) curve is to the green solid (dashed) curve). Similar curves demonstrating anticrossings were produced by Moroz and Barnes [37] and Mireles and Kirczenow [50] for the strong spin–orbit coupling case, but without the application of external magnetic fields. Our study shows that spin textures still exist even if external magnetic fields are applied in the transverse (x), parallel (y), or perpendicular (z) directions to the wire.

3.2.2 Parallel (y) magnetic field

The evolution of dispersions for strong Rss and magnetic field applied in the y direction are shown in Fig. 3.3. Non–parabolicities (spin textures) in the dispersions (even at zero magnetic field) are noticeable, especially in the first three spin–split subbands (see plot (a) in Fig. 3.3). However, band maxima at $k_y = 0$ are absent in these dispersions as the presence of Rashba intersubband coupling tends to smooth out the dispersions at very small wavevectors. These results confirm with those presented by Serra et al [26] for fields applied parallel to the wire in the presence of Rashba intersubband coupling as pointed out in Section 3.1.

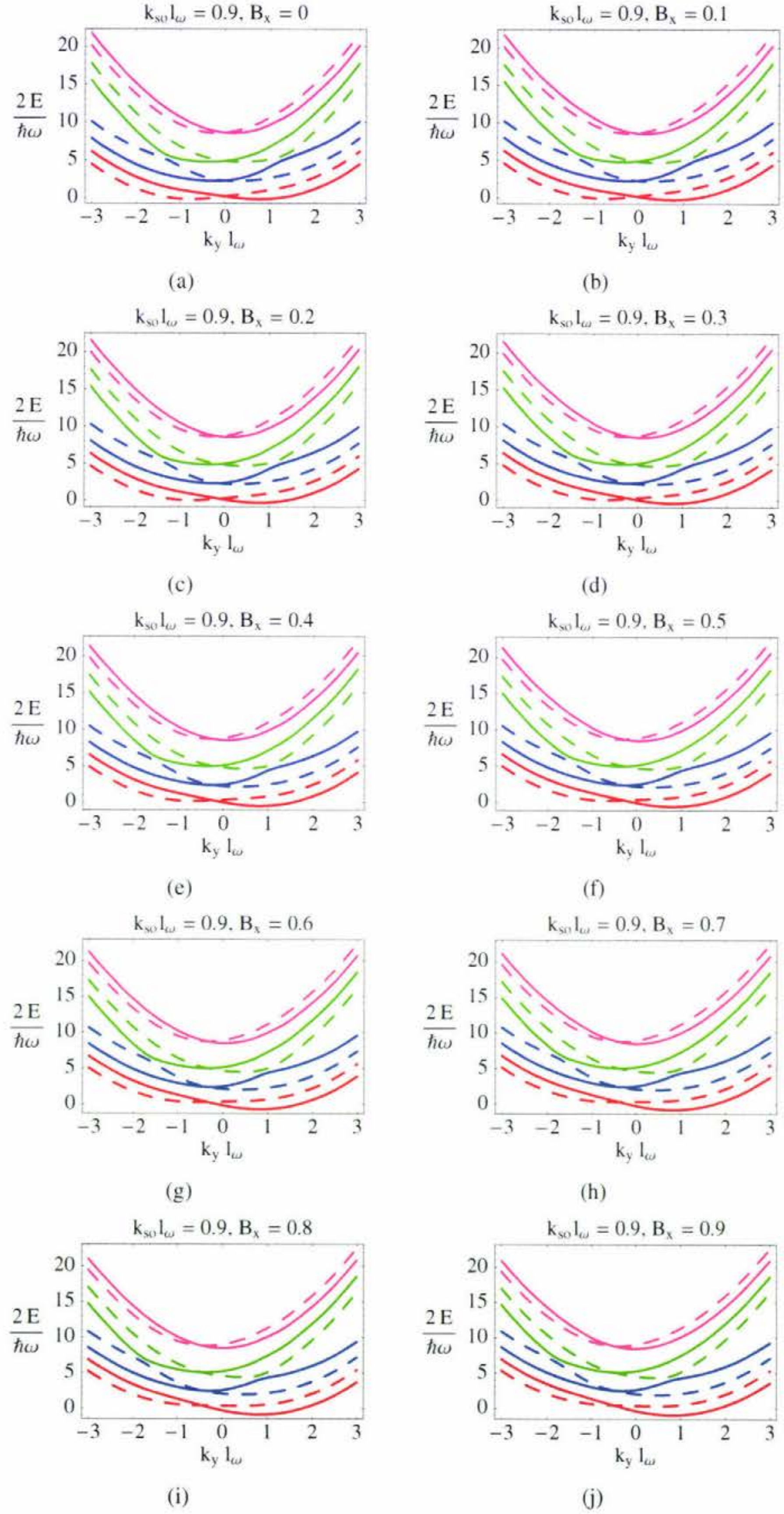

$k_{so} l_\omega = 0.9$, $B_x = 0$

(a)

$k_{so} l_\omega = 0.9$, $B_x = 0.1$

(b)

$k_{so} l_\omega = 0.9$, $B_x = 0.2$

(c)

$k_{so} l_\omega = 0.9$, $B_x = 0.3$

(d)

$k_{so} l_\omega = 0.9$, $B_x = 0.4$

(e)

$k_{so} l_\omega = 0.9$, $B_x = 0.5$

(f)

$k_{so} l_\omega = 0.9$, $B_x = 0.6$

(g)

$k_{so} l_\omega = 0.9$, $B_x = 0.7$

(h)

$k_{so} l_\omega = 0.9$, $B_x = 0.8$

(i)

$k_{so} l_\omega = 0.9$, $B_x = 0.9$

(j)

Figure 3.2: The evolution of dispersions for strong Rss and magnetic field applied in the transverse (x) direction in the full Rashba wire model.

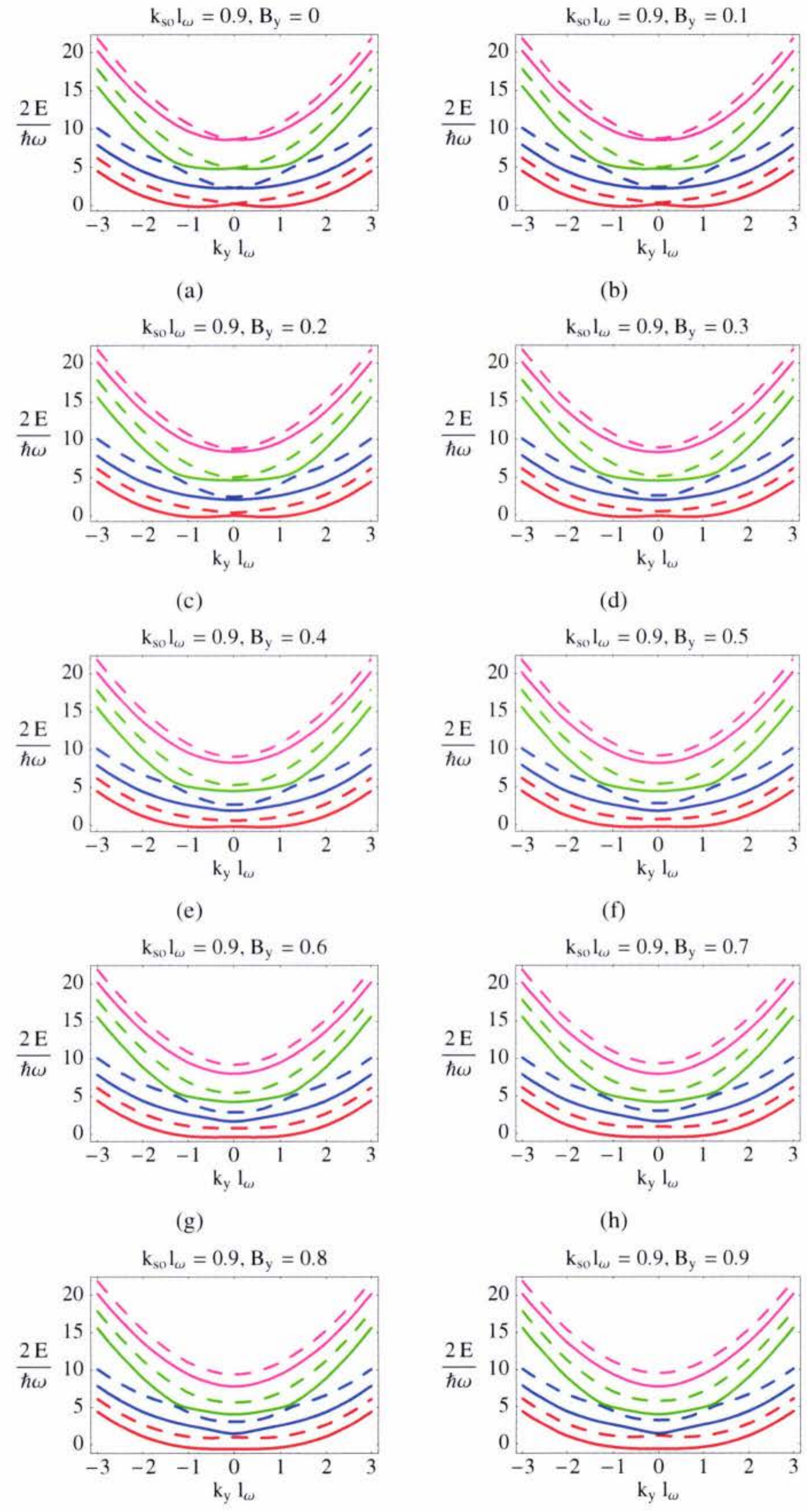

$k_{so} l_\omega = 0.9$, $B_y = 0$ (a)

$k_{so} l_\omega = 0.9$, $B_y = 0.1$ (b)

$k_{so} l_\omega = 0.9$, $B_y = 0.2$ (c)

$k_{so} l_\omega = 0.9$, $B_y = 0.3$ (d)

$k_{so} l_\omega = 0.9$, $B_y = 0.4$ (e)

$k_{so} l_\omega = 0.9$, $B_y = 0.5$ (f)

$k_{so} l_\omega = 0.9$, $B_y = 0.6$ (g)

$k_{so} l_\omega = 0.9$, $B_y = 0.7$ (h)

$k_{so} l_\omega = 0.9$, $B_y = 0.8$ (i)

$k_{so} l_\omega = 0.9$, $B_y = 0.9$ (j)

Figure 3.3: The evolution of dispersions for strong Rss and magnetic field applied in the parallel (y) direction in the full Rashba wire model.

3.2.3 Perpendicular (z) magnetic field

Figure 3.4 shows the evolution of dispersions for strong Rss and for magnetic field applied in the z direction. Spin textures are seen in the dispersions due to the Rashba intersubband coupling noticeable in the first three split subbands (Fig. 3.4). Similar to the dispersions obtained for fields applied in the y direction (i.e., Fig. 3.3), there are no significant energy gaps noticeable at $k_y = 0$.

The characteristic differences that arises in the dispersions at each magnetic field direction directly determines the characteristics of their corresponding differential conductance, which are presented in Chapter 4.

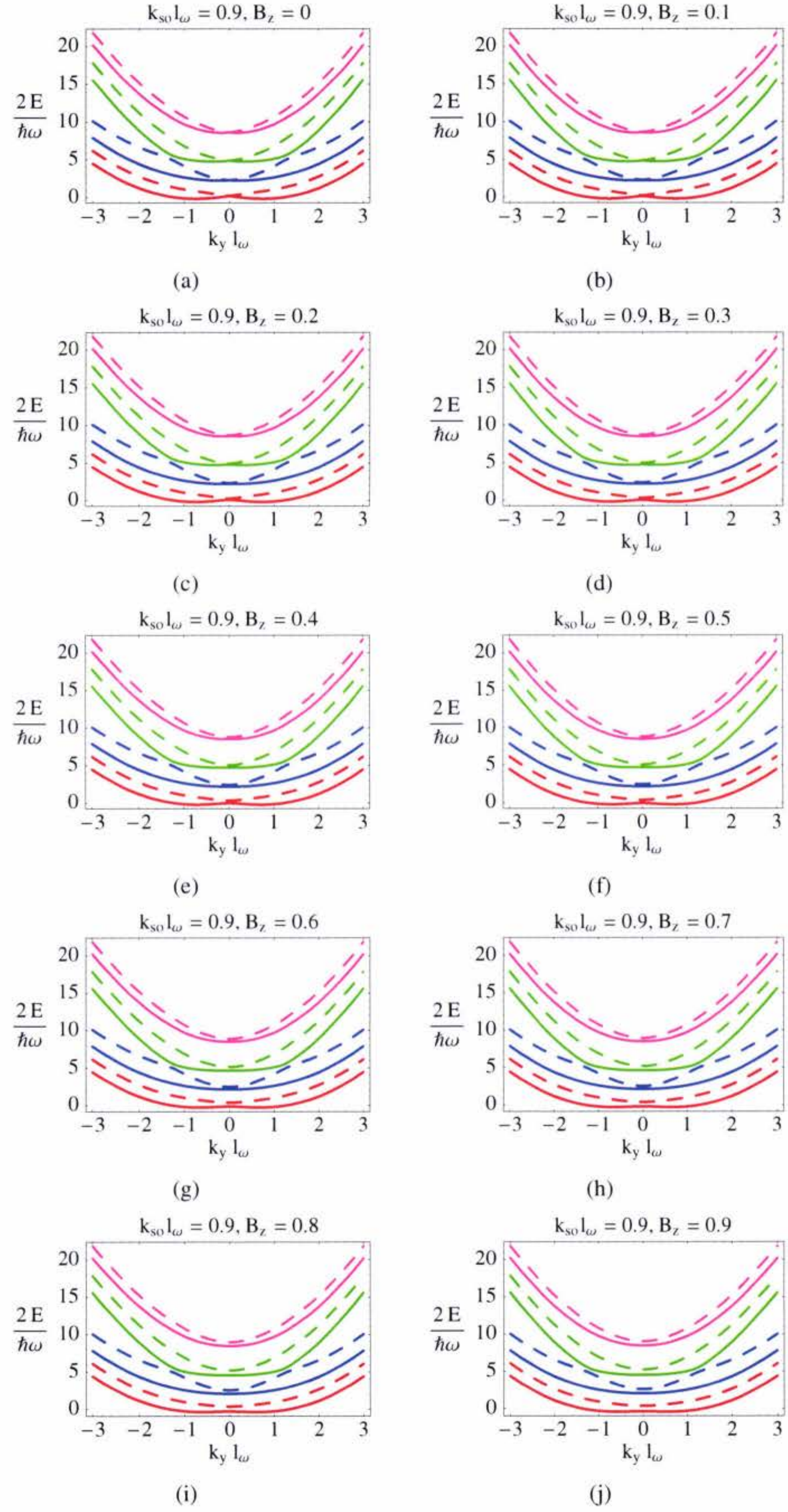

(a) (b) (c) (d) (e) (f) (g) (h) (i) (j)

Figure 3.4: The evolution of dispersions for strong Rss and magnetic field applied in the perpendicular (z) direction in the full Rashba wire model.

Chapter 4

Differential Conductance

This Chapter presents and also discusses the differential conductance results for the quantum wire. The results are organised according to normal and full Rashba and are presented in three sets, each for magnetic field directions transverse (x), parallel (y), and perpendicular (z) to the wire. For each field direction the differential conductance results are displayed for zero and strong Rss scenarios for an arbitrary Fermi level through three different types of plots, namely density, parametric3D, and 2D.

The density plots qualitatively shows the differential conductance profile as a function of V_{sd} (through V) and magnetic field both varied in the range 1 to 10. The density plots are colour scaled where lighter shades of red correspond to maximum conductance. For magnetic field applied in the transverse (x) direction in the normal Rashba regime two types of parametric3D plots are shown. One of these shows the variation of differential conductance with V_{sd} varied in the range 0 to 10 at fixed magnetic fields from 1 to 5 (in steps of 1). The other shows the same, but with magnetic field varied in the range 1 to 10 at fixed V_{sd}. For the rest of the sets only the variation of differential conductance with V_{sd} at fixed magnetic fields are shown. There are two types of 2D plots presented for magnetic field applied in the transverse (x) direction only (for both normal and full Rashba regimes). One of these shows the variation of differential conductance with V_{sd} in the range 0 to 10 at zero magnetic field while the other shows the same with magnetic field at zero V_{sd}.

The results are presented in Section 4.1 highlighting the discernible features followed by a discussion of these features emphasising the new results in Section 4.2.

4.1 Differential conductance results

4.1.1 Normal Rashba differential conductance

The differential conductance plots shown in this section are for the normal Rashba wire model (without Ric). Since the dispersions for fields applied in the parallel (y) and perpendicular (z) directions are exactly the same the differential conductance plots for these field directions are identical. For this reason only the differential conductance results for field applied parallel to the wire are shown. A significant finding evident from the results presented in this Section is that for fields applied in the parallel (and perpendicular) directions the overall conductance is greatly reduced (attributed to the presence of energy gaps in the band structure).

Set 1: Transverse (x) magnetic field

Figures 4.1, 4.2, and 4.3 presents the density, parametric3D, and 2D differential conductance results, respectively, for the wire with magnetic field applied in the x direction. Clear differences in the conductance profiles can be seen by comparing the density plots for zero Rss (i.e., plot (a)) and strong Rss (plot (b)) in Fig. 4.1. The presence of more lighter shades in the latter plot at low fields indicate that conductance is enhanced for a greater range of bias voltages in the strong Rashba limit than in the zero Rashba limit. This effect is profound for fields applied in the parallel (and perpendicular) directions (see Fig. 4.4). By inspecting plot (c) in Fig. 4.2 one can see the presence of instantaneous peaks in conductance within low to mid range bias voltages at high magnetic fields even though the overall conductance is low. While at large voltages a reduction in conductance at low fields is observed. In Fig. 4.2 plots (b) and (d) clearly shows that as the magnetic field increases the conductance decreases at fixed voltages. The decrease in conductance with increasing magnetic field is known as magnetic depopulation and have been reported in other works (see Section 1.3.2 in Chapter 1). This particular variation in conductance is universally seen at all applied magnetic field directions and even for zero and strong Rss scenarios in both Rashba regimes. For this reason these plots are only shown for field applied in the transverse (x) direction in the normal Rashba regime.

Set 2: Parallel (y) and perpendicular (z) magnetic field

Figures 4.4 and 4.5 presents the density and parametric3D differential conductance results, respectively, for magnetic field applied in the parallel (y) direction. As the dispersion relations between fields applied in the transverse and parallel (and perpendicular) directions in the strong Rashba limit differ greatly (see Fig. 3.1), their corresponding differential conductance plots are significantly modified. These differences in the differential conductance plots can be seen by examining for example, plots (b) in Figs. 4.1 and 4.4, plot (c) in Fig. 4.2, and plot (b) in Fig. 4.5. The main difference between plots (a) and (b) in Fig. 4.5 is that there is significant suppression in the overall conductance in the strong Rashba limit. The "local" conductance, however, is still enhanced at very low fields and upto a greater range of voltages in the strong Rashba limit.

4.1.2 Full Rashba differential conductance

The differential conductance plots shown in this Section belong to the full Rashba wire model (includes Ric). Several features can be observed by comparing the differential conductance plots between each field direction and Rashba regimes.

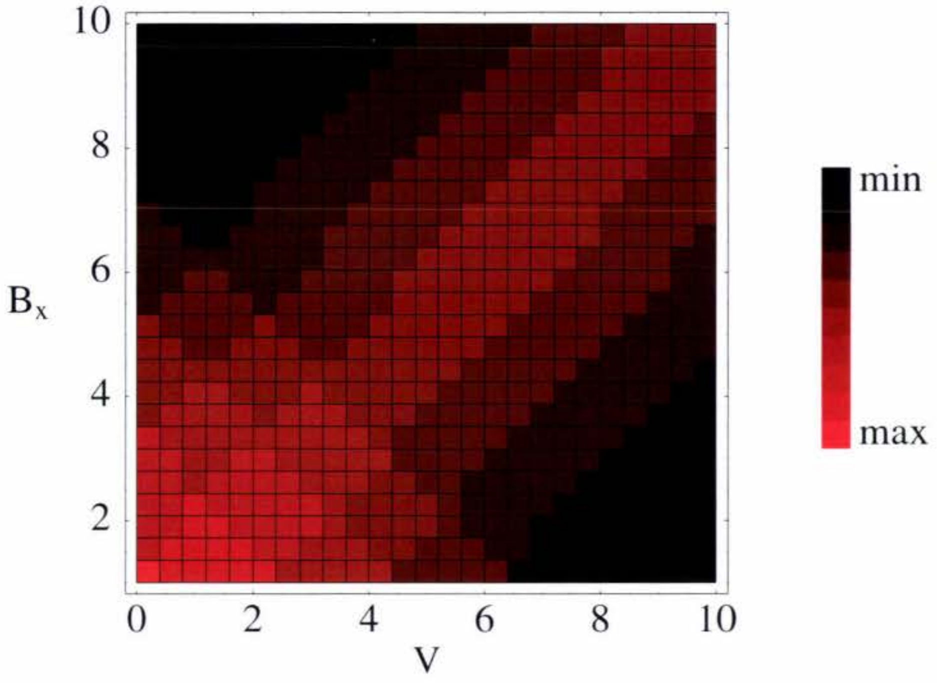

(a) Zero Rss

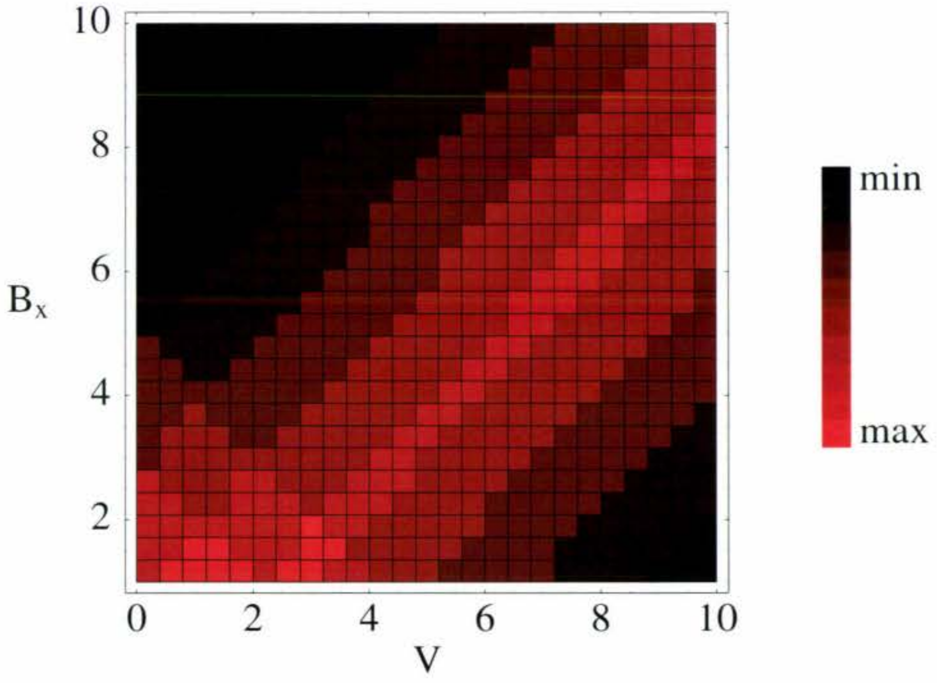

(b) Strong Rss

Figure 4.1: Density ΔG plots for transversely applied magnetic field B_x at zero and strong Rss in the normal Rashba wire model.

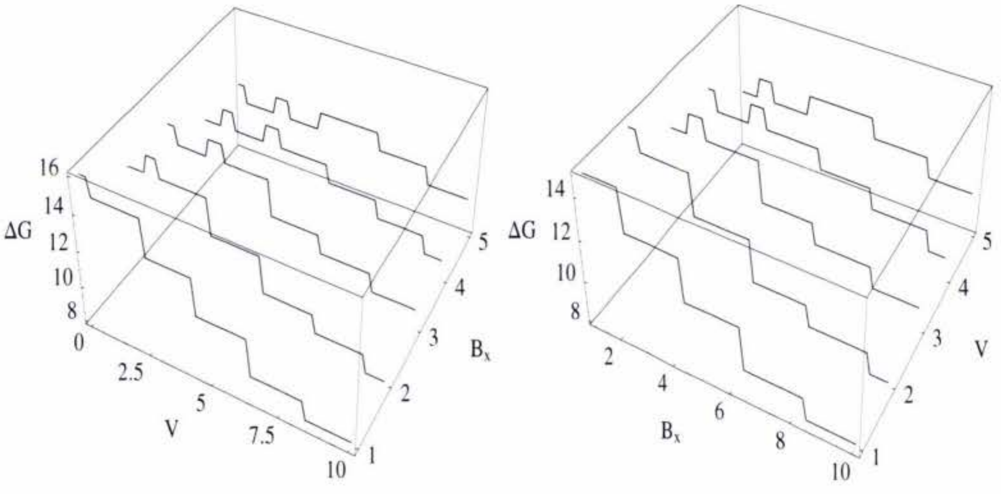

(a) Zero Rss (b) Zero Rss

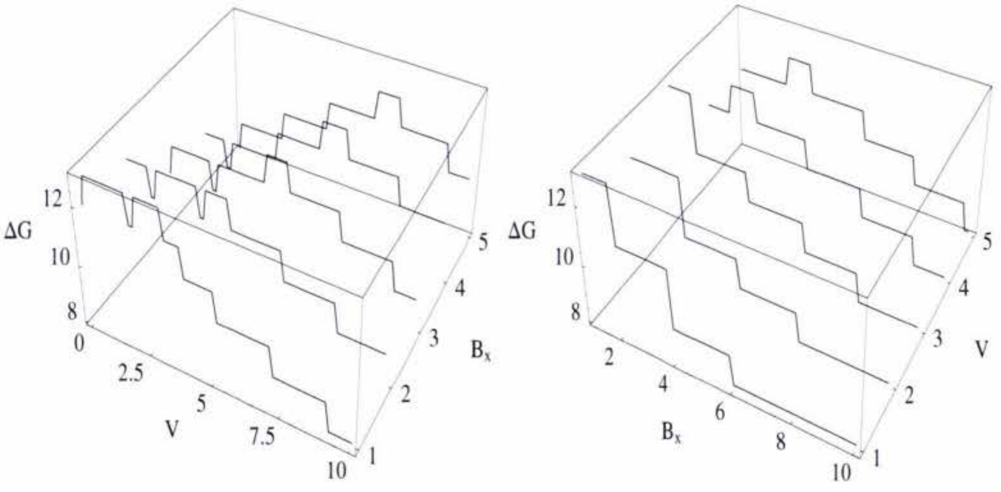

(c) Strong Rss (d) Strong Rss

Figure 4.2: Parametric3D ΔG plots as a function of V_{sd} at fixed transverse magnetic field B_x and as a function of B_x at fixed V_{sd} for zero and strong Rss in the normal Rashba wire model.

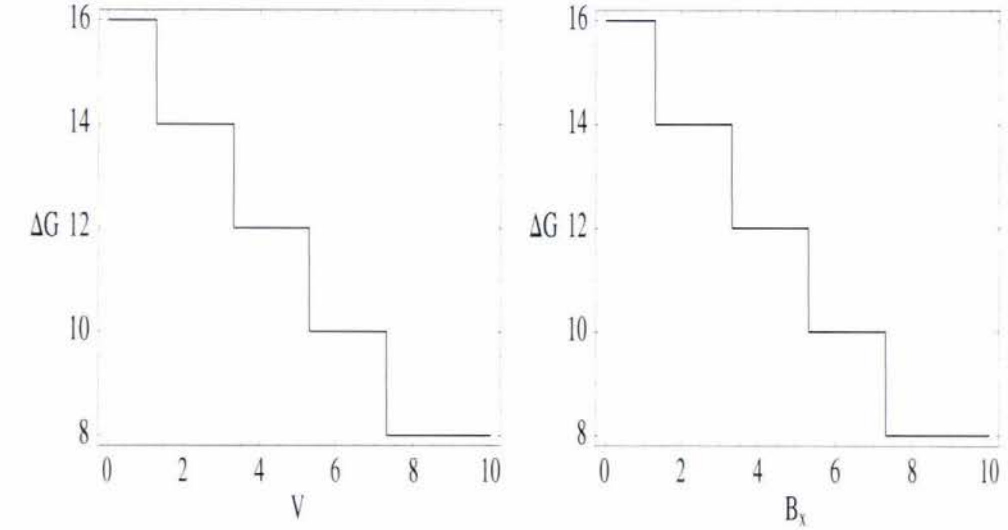

(a) Zero Rss (b) Zero Rss

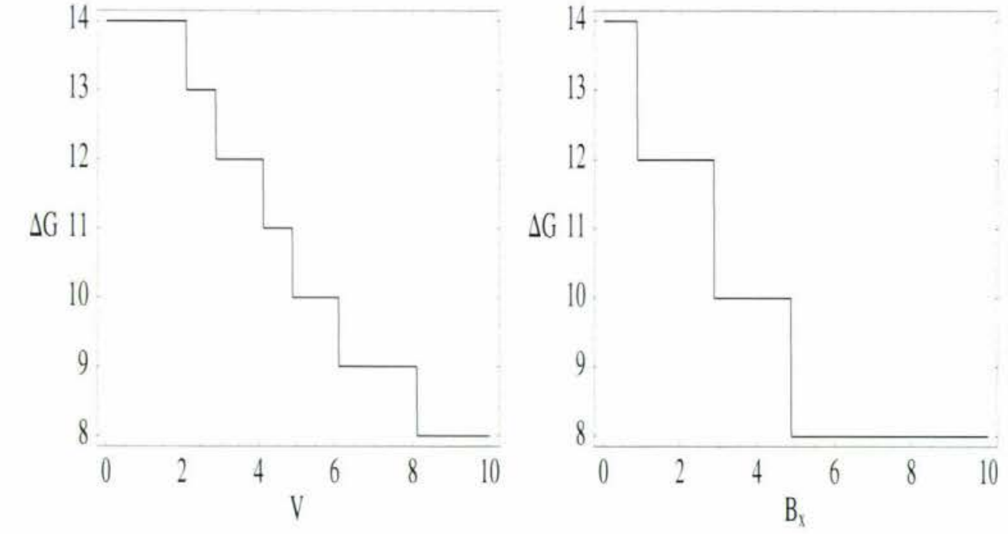

(c) Strong Rss (d) Strong Rss

Figure 4.3: 2D ΔG plots as a function of V_{sd} at zero transverse magnetic field B_x and as a function of B_x at zero V_{sd} for zero and strong Rss in the normal Rashba wire model.

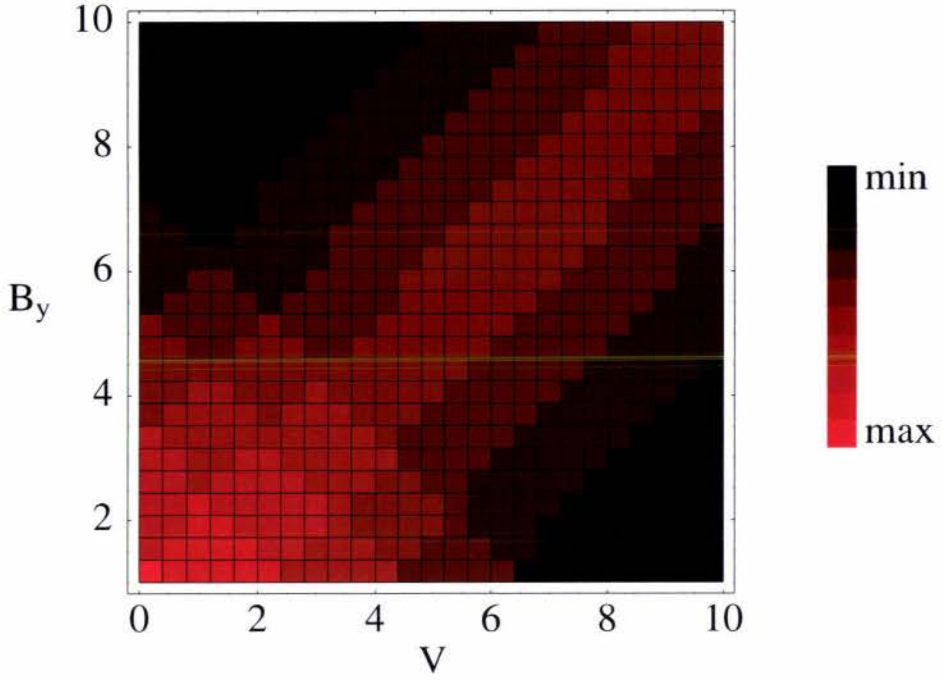

(a) Zero Rss

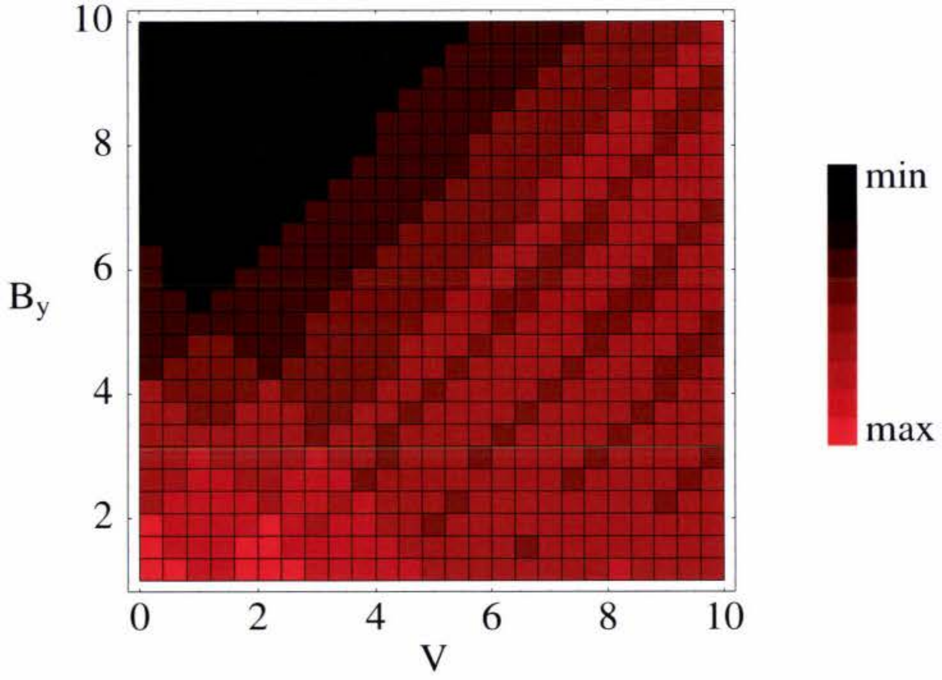

(b) Strong Rss

Figure 4.4: Density ΔG plots for parallelly applied magnetic field B_y for zero and strong Rss in the normal Rashba wire model.

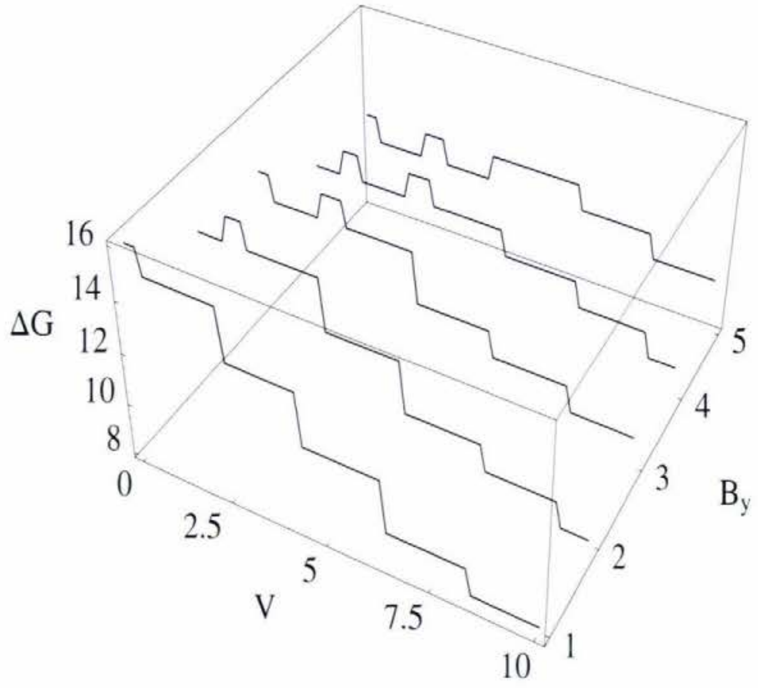

(a) Zero Rss

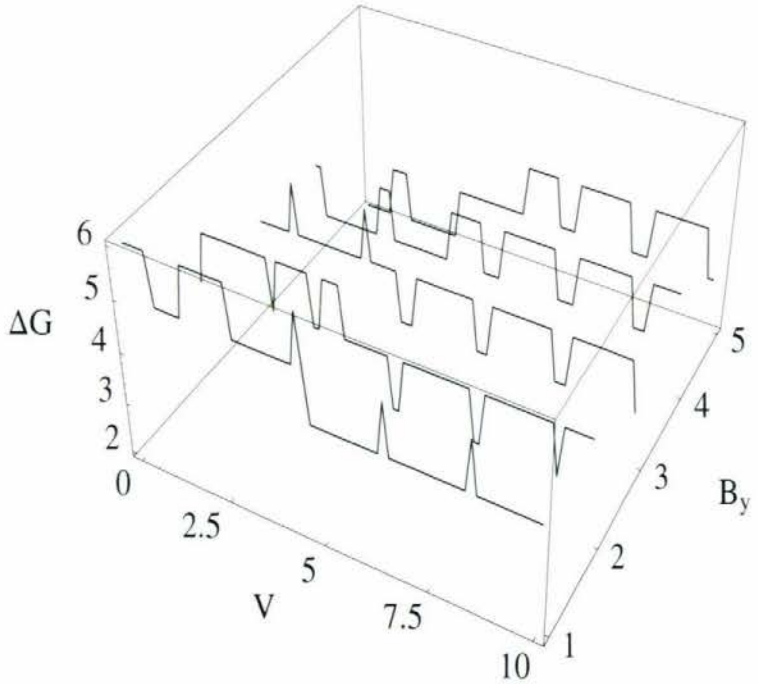

(b) Strong Rss

Figure 4.5: Parametric3D ΔG plots as a function of V_{sd} at fixed parallel magnetic field B_y for zero and strong Rss in the normal Rashba wire model.

Set 1: Transverse (x) magnetic field

Figures 4.6, 4.7, and 4.8 presents the density, parametric3D, and 2D differential conductance results, respectively, for magnetic field applied in the transverse (x) direction. The only discernible feature obtained by comparing for example, plot (c) in Fig. 4.2 and plot (b) in Fig. 4.7 (in the strong Rashba limit) indicates that at low fields and low voltages local conductance is only slightly reduced in the full Rashba model. There are hardly any other significant features depicted between the differential conductance plots in both Rashba regimes. This result indicates that Rashba intersubband coupling hardly has any significant bearing on the differential conductance for fields applied in the transverse (x) direction in the strong Rashba limit. Comparing plots (a) and (b) in Fig. 4.6 indicates that local conductance is enhanced upto mid range fields and mid range voltages in the strong Rashba limit. This feature is also seen for fields applied in the parallel and perpendicular directions in the strong Rashba limit for the full Rashba model. The overall conductance is still greater in the zero Rashba limit at low magnetic fields and low bias voltages.

Set 2: Parallel (y) magnetic field

Figures 4.9 and 4.10 shows the density and parametric3D differential conductance results, respectively, for magnetic field applied in the parallel (y) direction. By comparing plot (b) in Figs. 4.4 and 4.9 (in the strong Rashba limit) it is seen that conductance is enhanced upto mid range magnetic fields and mid range voltages in the full Rashba model. It is confirmed by inspecting plot (b) in Figs. 4.5 and 4.10 that there is no suppression in conductance in the full Rashba model in the strong Rashba limit unlike for the same situation in the normal Rashba model. These results indicate that in the presence of Rashba intersubband coupling and for fields applied parallel to the wire the overall conductance is not significantly reduced for low fields and low voltages in the full Rashba model.

Set 3: Perpendicular (z) magnetic field

Figures 4.11 and 4.12 shows the density and parametric3D differential conductance results, respectively, for magnetic field applied in the perpendicular (z) direction. In the presence of Rashba intersubband coupling even for fields applied perpendicular to the wire there is no suppression in the overall conductance. A result similar to those obtained for fields applied in the parallel direction to the wire in the full Rashba model. Local conductance is enhanced upto mid range fields and mid range voltages in the strong Rashba limit in the full Rashba model (unlike for the same situation in the normal Rashba model). The overall conductance is still greater at low fields and low voltages in the zero Rashba limit (see plot (a) and (b) in Fig. 4.11).

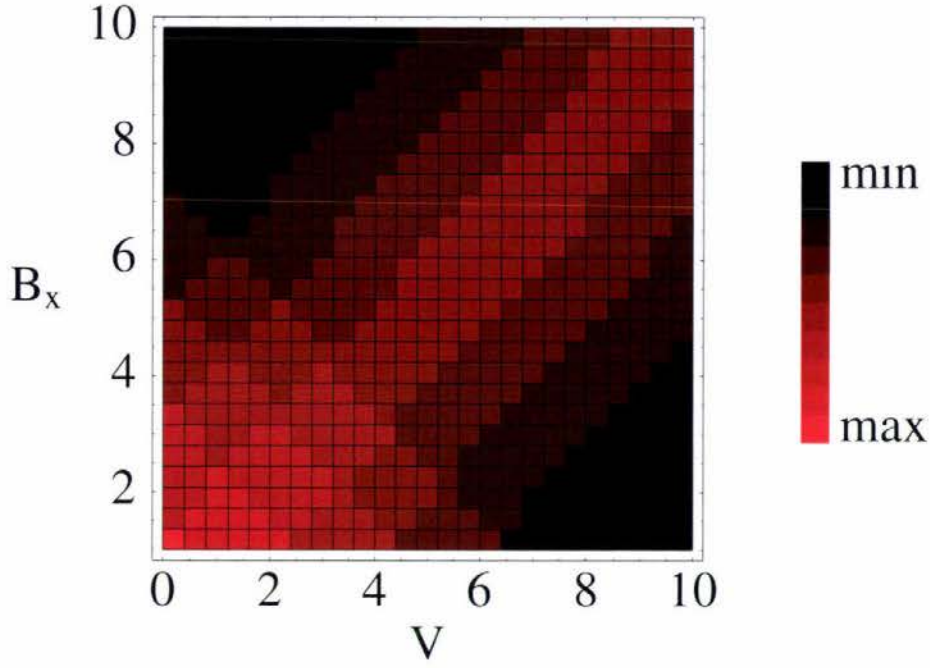

(a) Zero Rss

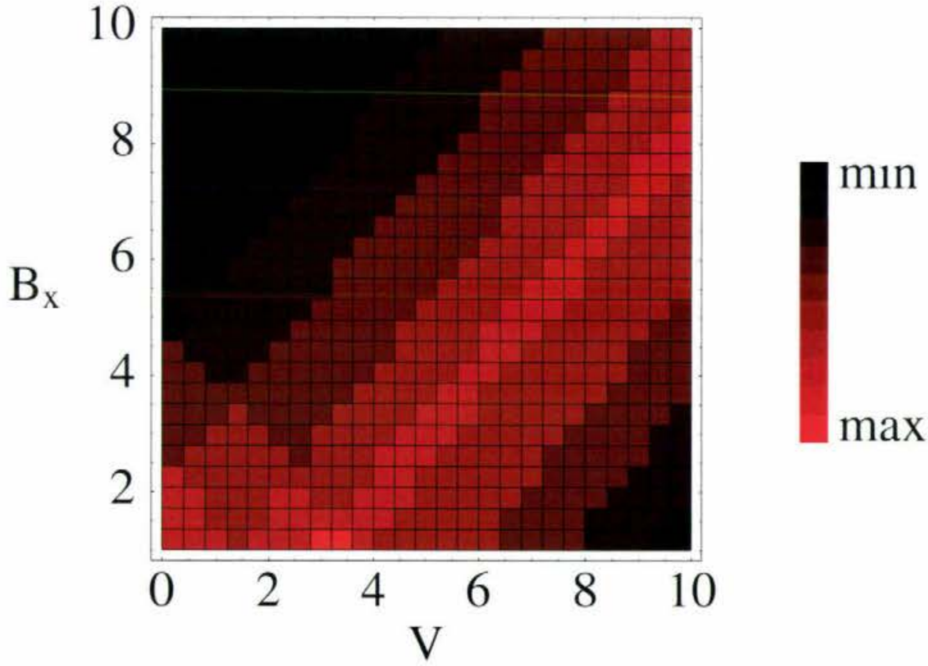

(b) Strong Rss

Figure 4.6: Density ΔG plots for transversely applied magnetic field B_x for zero and strong Rss in the full Rashba wire model.

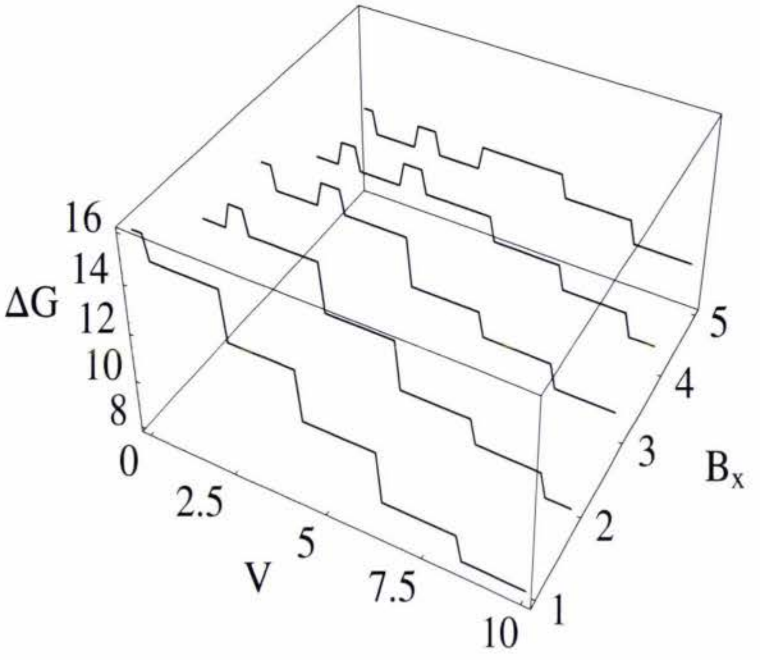

(a) Zero Rss

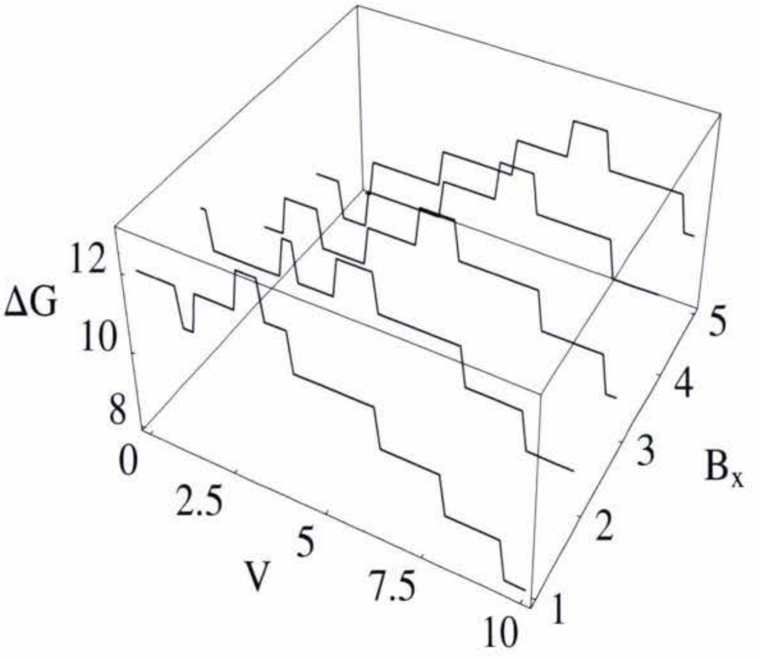

(b) Strong Rss

Figure 4.7: Parametric3D ΔG plots as a function of V_{sd} at fixed transverse magnetic field B_x for zero and strong Rss in the full Rashba wire model.

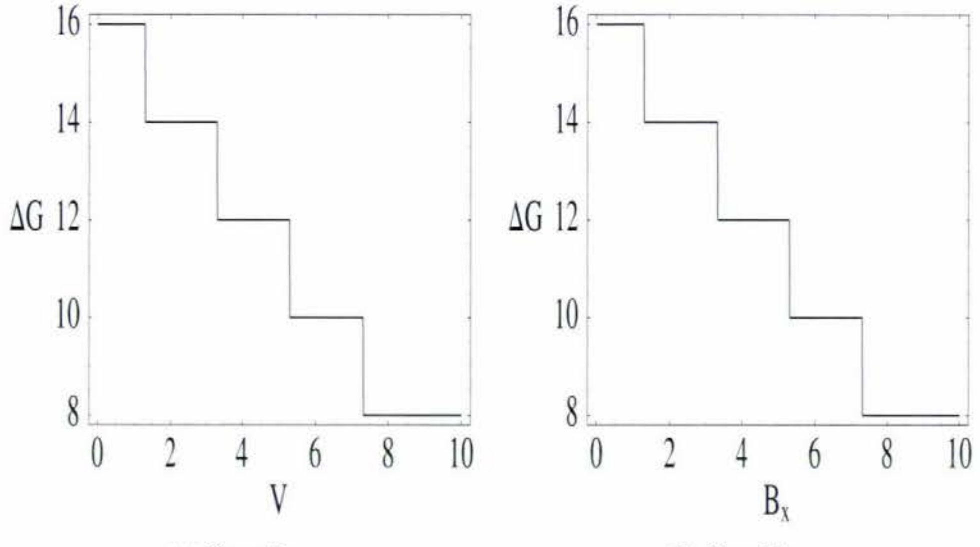

(a) Zero Rss (b) Zero Rss

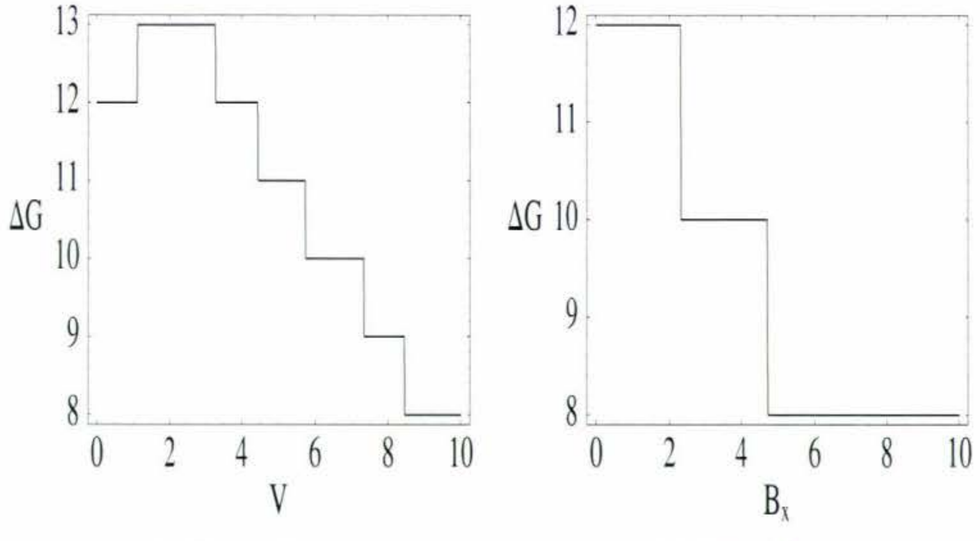

(c) Strong Rss (d) Strong Rss

Figure 4.8: 2D ΔG plots as a function of V_{sd} at zero transverse magnetic field B_x and as a function of B_x at zero V_{sd} for zero and strong Rss in the full Rashba wire model.

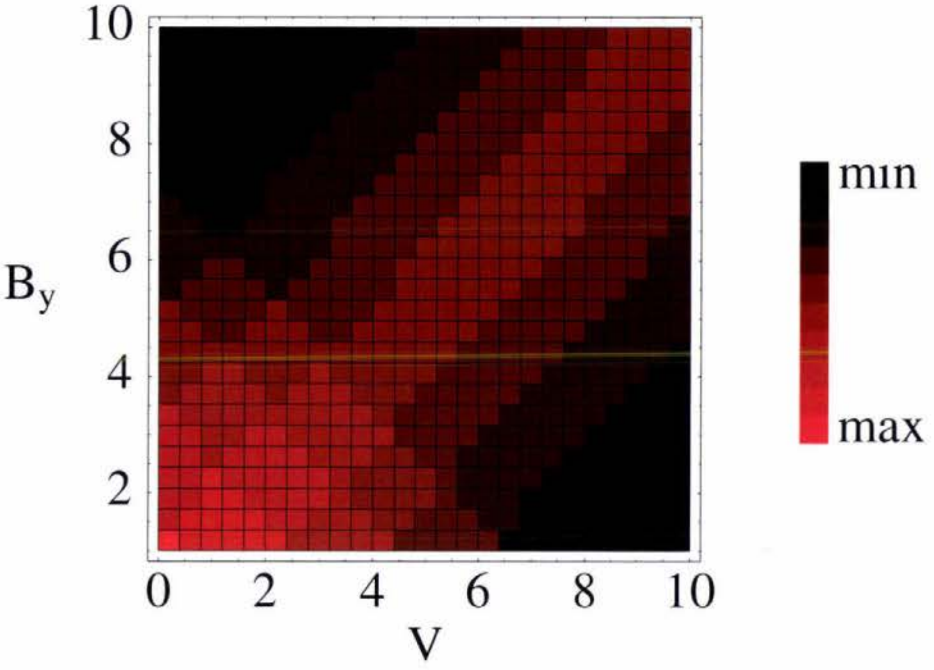

(a) Zero Rss

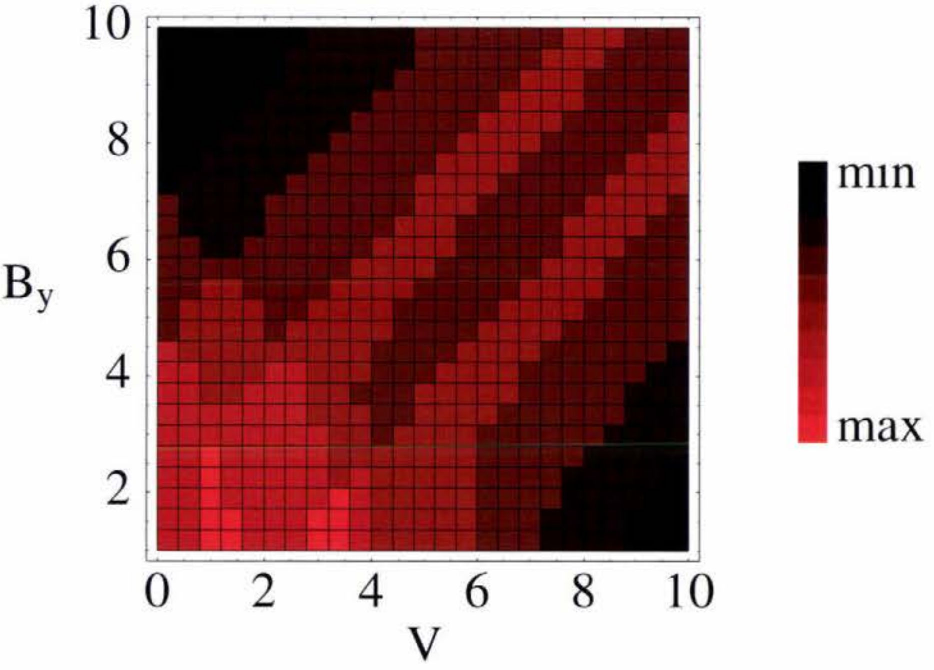

(b) Strong Rss

Figure 4.9: Density ΔG plots for parallelly applied magnetic field B_y for zero and strong Rss in the full Rashba wire model.

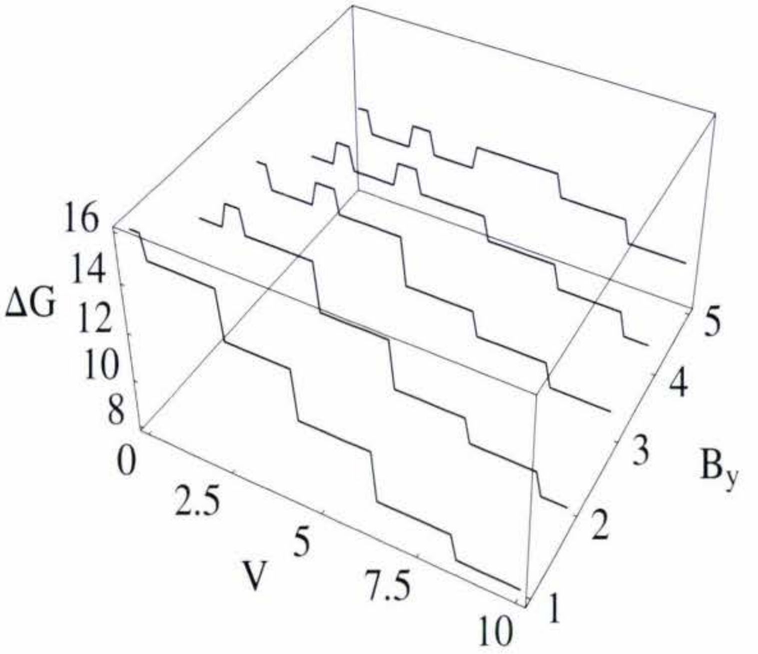

(a) Zero Rss

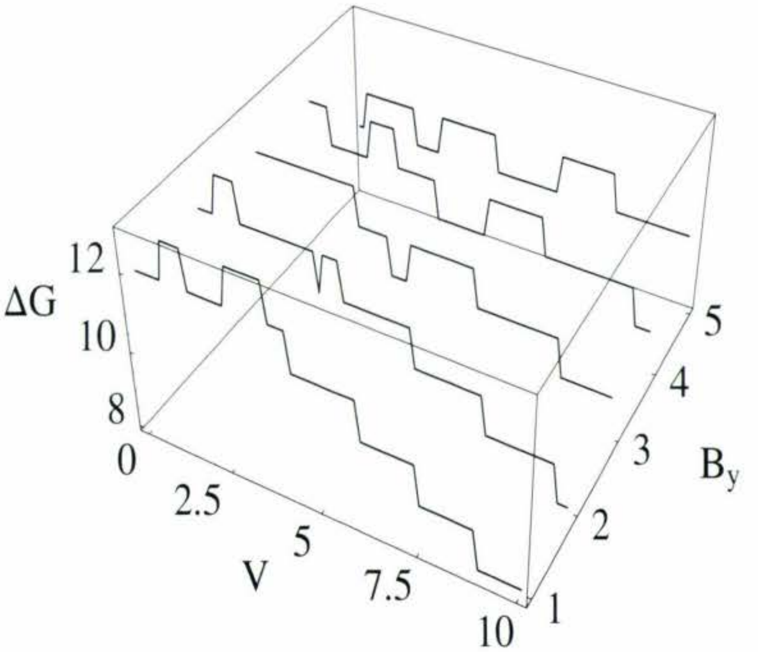

(b) Strong Rss

Figure 4.10: Parametric3D ΔG plots as a function of V_{sd} at fixed parallel magnetic field B_y for zero and strong Rss in the full Rashba wire model.

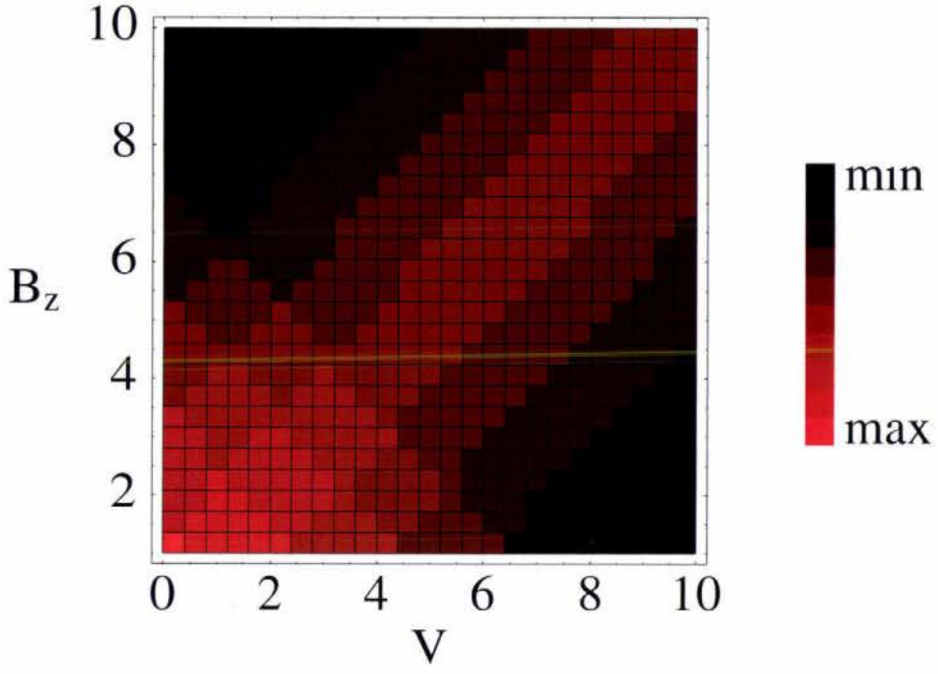

(a) Zero Rss

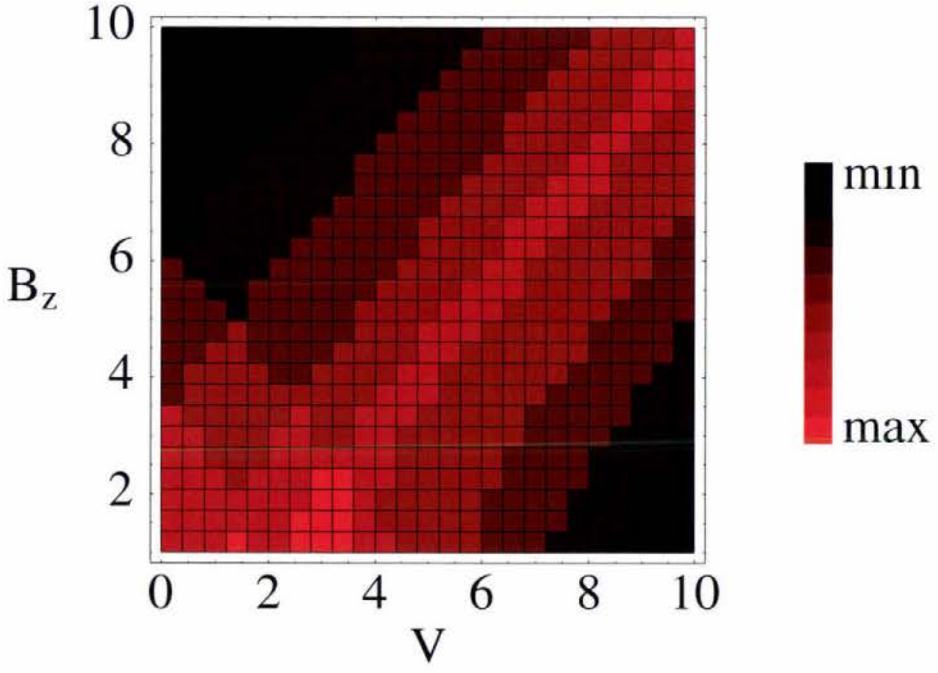

(b) Strong Rss

Figure 4.11: Density ΔG plots for perpendicularly applied magnetic field B_z for zero and strong Rss in the full Rashba wire model.

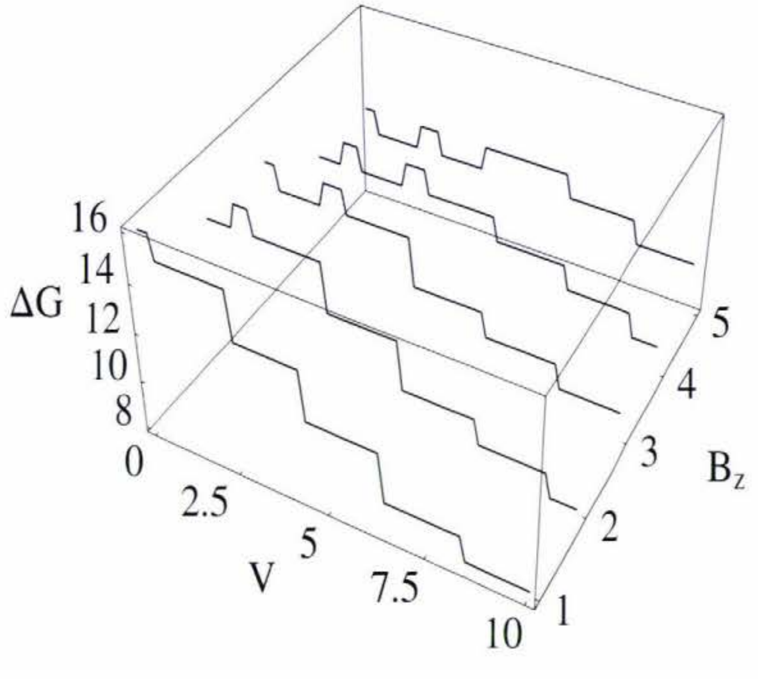

(a) Zero Rss

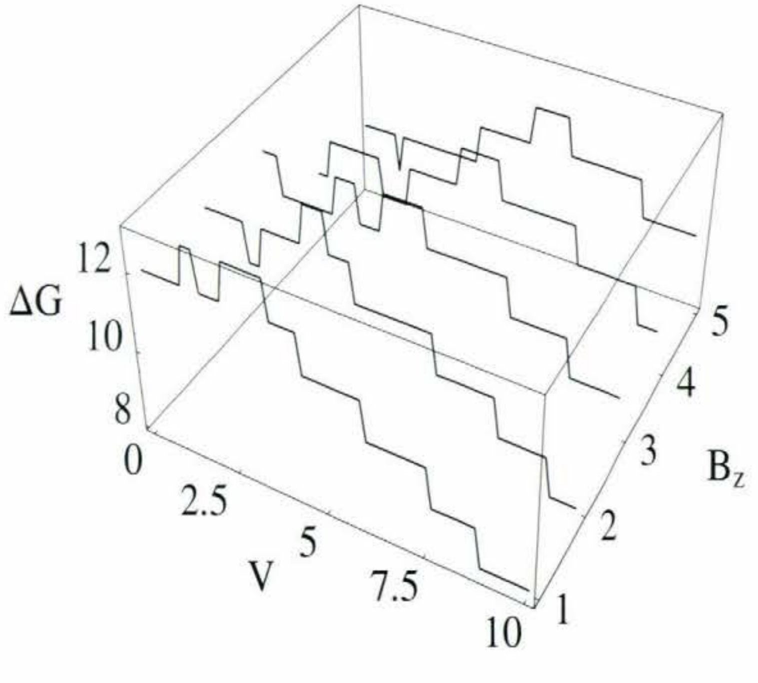

(b) Strong Rss

Figure 4.12: Parametric3D ΔG plots as a function of V_{sd} at fixed perpendicular magnetic field B_z for zero and strong Rss in the full Rashba wire model.

4.2 Discussion

The differential conductance results presented in Section 4.1 are new for the ballistic quantum wire studied in this work as no previous studies have produced a theoretical calculation showing the variation of differential conductance with source–drain voltages, application of external magnetic fields (in all three spatial directions), and at zero and strong Rashba spin–orbit interaction situations. In this Section an attempt is made to explain and discuss the inherent features displayed by the differential conductance results.

Figure 4.13 is used to explain how the differential conductance arises for zero and strong Rss scenarios at zero and increasing bias voltage and magnetic field situations. The schematic illustrates how subbands get filled or emptied as the electrochemical potentials on the left (source) μ_L and right (drain) μ_R changes as the source–drain bias is varied. Electron states are characterised by their group velocities

$$v_g = \hbar^{-1}\frac{\partial E}{\partial k} \tag{4.1}$$

where right moving states have positive and left have negative velocities.

At zero Rss, zero bias, and zero magnetic field (i.e., no Zss) all states below the Fermi level (E_F) are occupied (shown by closed circles) and those above are empty (open circles). This scenario is illustrated in plot (a) in Fig. 4.13 shown for four degenerate subbands. Each occupied unsplit subband corresponds to a conductance level of $2e^2/h$. When V_{sd} is changed (at zero field and zero Rashba) the left and right moving states get depleted or occupied as the left and right quasi–Fermi level changes according to Eq. 2.39. This situation is depicted in plot (b) in Fig. 4.13. Hence, conductance changes accordingly in full steps as the quasi–Fermi level passes each subband.

Plots (a) and (b) in Fig. 4.3 show the variation of differential conductance in steps with increasing bias voltage (at zero field) and increasing field (at zero bias voltage), respectively, for the zero Rss scenario. While plot (c) and (d) in Fig. 4.3 show the same but for strong Rss. The 2D differential conductance plots are only shown for the transverse (x) field direction for both normal and full Rashba regimes, because the qualitative features shown by these 2D plots are similar to those for the other field directions in the same regime. At zero field since the dispersions in the normal Rashba regime (plot (a) in Fig. 3.1) are the same for each field direction, their corresponding zero field 2D differential conductance plots are the same (plot (c) in Fig. 4.3). In the full Rashba regime the zero field dispersions for fields applied in the parallel and perpendicular directions are the same (see plot (a) in Figs. 3.3 and 3.4) and thus their zero field 2D differential conductance plots are the same.

At strong Rss and in the presence of a magnetic field applied in some arbitrary direction as each subband splits, these spin–split states contribute differently to the conductance as the states get populated or depopulated as the source–drain bias changes. Each spin–split subband contributes $e^2/2$ to the conductance. In plot (c) in Fig. 4.13 a scenario for strong Rss and strong field applied in the x direction corresponding to the dispersion seen in plot (b) in Fig. 3.1 is shown as an example to explain how the differential conductance arises for this case. As V_{sd} is varied increasing the right level allows more right moving states to get occupied, while more left moving states get emptied as the left level decreases. As the right level rises above the successive right moving states the conductance increases by half a step, while conductance decreases by half a step as the left level falls below the left moving states. Plot (d) in Fig. 4.13 represents a scenario where only Zeeman spin splitting is present at zero bias. With increasing magnetic field as the subbands split and move above (or below) the Fermi level, states get depopulated (populated). The zero bias 2D differential conductance that arises due to this mechanism is shown in plot (b) in Fig. 4.3.

As the magnetic field changes in value and direction for zero and strong Rss scenarios the subbands are split in different ways. As the dispersions change, the left and right moving states are depleted or occupied differently as V_{sd} is varied. By this mechanism peaks in the differential conductance arises, for example as seen in the respective density differential conductance profiles as different shading patterns.

A distinctive feature universally exhibited by all the density plots is the formation of two branches (alternate shades) as subbands split due to an increasing magnetic field (Zss), seen for all magnetic field directions. Another universal feature seen in the zero Rashba limit is that the overall conductance is greater at low fields and low bias voltages for all field directions and Rashba regimes. Conductance is greater because at low fields, low voltages, and zero (weak) Rashba spin splitting there are a larger number of occupied subbands present. As the field increases the increasing Zeeman effect shifts the split subbands away from the quasi–Fermi levels and therefore less available filled states reduces the conductance. This argument is also valid for strong Rashba spin splitting situations. Thus, weak Zeeman and weak Rashba spin–orbit effects seems to enhance the overall conductance for the wire.

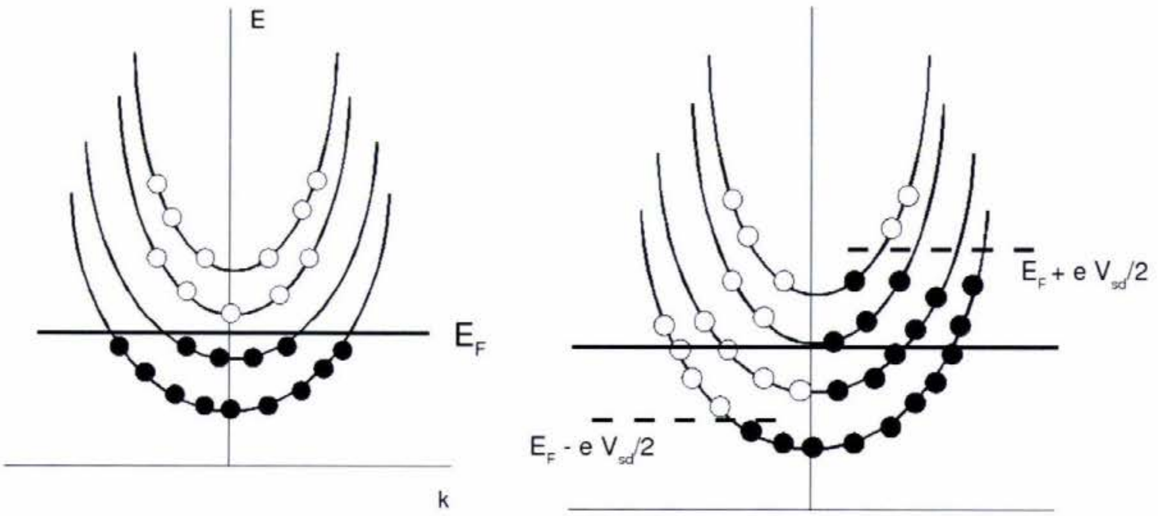

(a) Zero Rashba and Zeeman splitting, zero bias (b) Zero Rashba and Zeeman splitting, bias changed

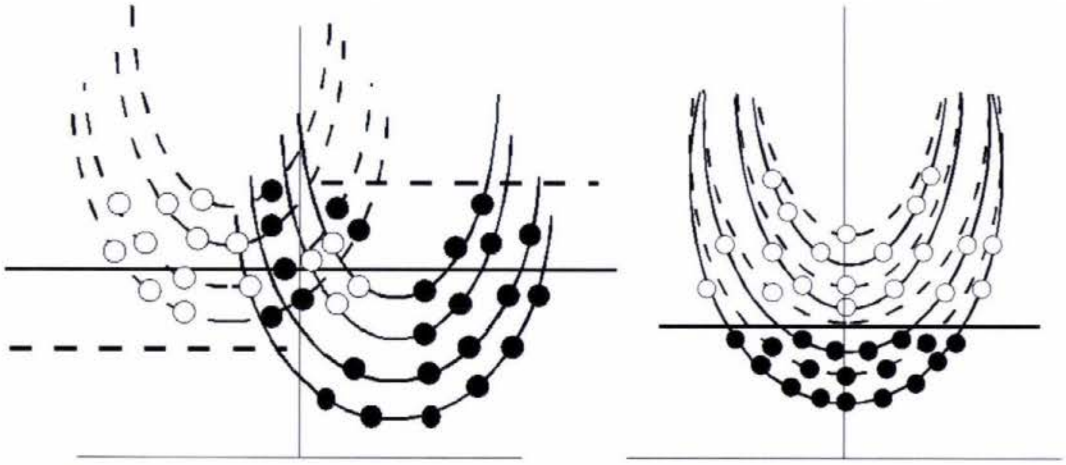

(c) Strong Rashba and Zeeman splitting, bias changed (d) Zeeman splitting only, zero bias

Figure 4.13: Schematic dispersions showing how states are filled and emptied with zero and changing source–drain bias voltage and different spin splitting scenarios (closed circles are occupied and open are empty states).

Chapter 5

Summary and Conclusion

In summary this thesis has calculated the theoretical differential conductance of a ballistic quantum wire in the presence of Rashba spin–orbit and Zeeman interactions. The Zeeman interaction is mediated by application of external magnetic fields in directions transverse (x), parallel (y), and perpendicular (z) to the wire axis. The thesis has also discussed the interplay between Rashba spin–orbit and Zeeman effects on the wire's dispersion and differential conductance. The wire was studied under two regimes, that is normal and full Rashba as represented by the Rashba spin–orbit interaction Hamiltonian. The normal Rashba regime models the wire without the Rashba intersubband coupling while the full Rashba model includes this coupling.

A numerical diagonalisation approach is used to solve an eigenvalue problem for the quantum wire to obtain the eigenenergy levels. From the energy levels dispersion relations are obtained for the two Rashba regimes at strong Rashba spin splitting and at the various magnetic field directions. The energy levels of the wire and the Landauer–Büttiker formalism is used to calculate the differential conductance. Differential conductance is calculated at zero and strong Rashba spin splitting scenarios for the various magnetic field directions and Rashba regimes. It is found that the direction of applied magnetic field in the strong spin–orbit interaction limit has significant effects on the dispersions and hence differential conductance.

The dispersion results for strong Rashba spin splitting and magnetic fields applied in the transverse direction in the normal Rashba regime reveals that a spin axis can be associated for all wavevectors; because in the absence of Rashba intersubband coupling the Rashba and Zeeman spins are parallel and does not give rise to mixed spin states. This conjecture, however, breaks down for strong Rashba spin splitting and fields applied in parallel (and perpendicular) directions for small wavevectors; because of the formation of band maxima and energy gaps around $k_y = 0$. These results are also consistent with the findings reported for example by Serra et al [26] and Pershin et al [45] for in–plane fields. Since our study also incorporated perpendicular magnetic fields we found existence of mixed spin states due to the presence of energy gaps in the strong Rashba limit, but in the absence of Rashba intersubband coupling even for perpendicularly applied fields.

A significant finding established from our work is that the overall conductance is greatly reduced due to the presence of energy gaps in the strong Rashba limit if Rashba intersubband coupling is not included in the wire model. Our work confirms that the formation of band maxima are suppressed for the wire in the full Rashba model (which includes Ric) in the strong Rashba limit applicable for fields in the parallel and perpendicular directions. Serra et al [26] reported this finding for a similar situation for in–plane (parallel) fields only. Thus, our study shows that inclusion of the full Rashba spin–orbit interaction Hamiltonian in the quantum wire model inhibits gap formation and henceforth reduction in the overall conductance in the strong Rashba limit at these field directions. The results also show that the overall conductance is greater at zero (and weak) Rashba spin splitting situations, low bias voltages, and low magnetic fields. It is therefore concluded that at low voltages conductance is enhanced at weak Zeeman and weak Rashba spin–orbit interaction effects. Local conductance is, however, enhanced in the strong Rashba limit at low fields, but for a greater range of bias voltages (in the normal regime) and upto mid range fields and mid range voltages in the full Rashba regime.

Besides the fundamental importance the results presented in this thesis of a ballistic quantum wire may be further used by experimentalists as a basis to design physical quantum wires for spin–based electronic devices in the near future. Furthermore, the work in this thesis can be extended to extract g-factors from the dispersion and differential conductance data. The thesis could be a basis for investigating similar electronic transport properties in ballistic quantum point contacts in the presence of Rashba spin–orbit and Zeeman interactions. Further to this, electron–electron interactions and temperature effects could be incorporated to investigate their effects on the dispersions and differential conductance.

Appendix A

Physical Hamiltonian expressions

This Appendix contains the expressions for the physical Hamiltonians for the quantum wire for both normal and full Rashba regimes and their corresponding eigenenergy expressions (for the normal Rashba model only) for each magnetic field direction (x, y, and z).

A.1 Normal Rashba Hamiltonian expressions

Magnetic field in x direction

Hamiltonian:

$$H_{qwnRasB_x} = \frac{p_x^2}{2m} + \frac{1}{2}m\omega_x^2 x^2 + \frac{\hbar^2 k_y^2}{2m} + \frac{\hbar^2 k_y k_{so}\sigma_x}{m} + \frac{1}{2}g\mu_B\sigma_x B_x \tag{A.1}$$

Eigenenergy expression:

$$\begin{aligned}
E_{n,k,\sigma} &= \hbar\omega_x(n+\frac{1}{2}) + \frac{\hbar^2 k_y^2}{2m} \pm \frac{\hbar^2 k_y k_{so}}{m} \pm \frac{1}{2}g\mu_B B_x \\
&= \frac{\hbar\omega_x}{2}(2n+1+\frac{\hbar k_y^2}{m\omega_x} \pm \frac{2\hbar k_y k_{so}}{m\omega_x} \pm \frac{g\mu_B B_x}{\hbar\omega_x}) \\
&= \frac{\hbar\omega_x}{2}(2n+1+k_y^2 l_\omega^2 \pm 2l_\omega^2 k_{so}k_y \pm \frac{B_x}{B_o}) \\
&= \frac{\hbar\omega_x}{2}(2n+1+k_y^2 l_\omega^2 \pm 2(k_{so}l_\omega)(k_y l_\omega) \pm B_x)
\end{aligned} \tag{A.2}$$

or

$$\frac{2E_{n,k,\sigma}}{\hbar\omega_x} = 2n+1+(k_y l_\omega)^2 \pm 2(k_{so}l_\omega)(k_y l_\omega) \pm B_x \tag{A.3}$$

where the following equations have been used to simplify the dispersion expressions;

$$l_\omega = \sqrt{\frac{\hbar}{m\omega_x}},\ B_o = \frac{\hbar\omega_x}{g\mu_B} = \frac{2\omega_x m_o}{ge}\ (\text{since}\ \mu_B = \frac{e\hbar}{2m_o}),\ \text{and}\ B_x \equiv \frac{B_x}{B_o}.$$

Magnetic field in y direction

Hamiltonian:

$$H_{qwnRasB_y} = \frac{p_x^2}{2m} + \frac{1}{2}m\omega_x^2x^2 + \frac{\hbar^2k_y^2}{2m} + \frac{\hbar^2k_yk_{so}\sigma_x}{m} + \frac{1}{2}g\mu_B\sigma_yB_y \tag{A.4}$$

Eigenenergy expression:

$$\frac{2E_{n,k,\sigma}}{\hbar\omega_x} = 2n + 1 + (k_yl_\omega)^2 \pm \sqrt{B_y^2 + 4(k_{so}l_\omega)^2(k_yl_\omega)^2}, \text{ where } B_y \equiv \frac{B_y}{B_o}. \tag{A.5}$$

Magnetic field in z direction

Hamiltonian:

$$H_{qwnRasB_z} = \frac{p_x^2}{2m} + \frac{1}{2}m\omega_x^2x^2 + \frac{\hbar^2k_y^2}{2m} + \frac{\hbar^2k_yk_{so}\sigma_x}{m} + \frac{1}{2}g\mu_B\sigma_zB_z \tag{A.6}$$

Eigenenergy expression:

$$\frac{2E_{n,k,\sigma}}{\hbar\omega_x} = 2n + 1 + (k_yl_\omega)^2 \pm \sqrt{B_z^2 + 4(k_{so}l_\omega)^2(k_yl_\omega)^2}, \text{ where } B_z \equiv \frac{B_z}{B_o}. \tag{A.7}$$

A.2 Full Rashba Hamiltonian expressions

Magnetic field in x direction

$$H_{qwfRasB_x} = \frac{p_x^2}{2m} + \frac{1}{2}m\omega_x^2x^2 + \frac{\hbar^2k_y^2}{2m} + \frac{\hbar^2k_yk_{so}\sigma_x}{m} - \frac{\alpha}{\hbar}\sigma_yp_x + \frac{1}{2}g\mu_B\sigma_xB_x \tag{A.8}$$

Magnetic field in y direction

$$H_{qwfullB_y} = \frac{p_x^2}{2m} + \frac{1}{2}m\omega_x^2x^2 + \frac{\hbar^2k_y^2}{2m} + \frac{\hbar^2k_yk_{so}\sigma_x}{m} - \frac{\alpha}{\hbar}\sigma_yp_x + \frac{1}{2}g\mu_B\sigma_yB_y \tag{A.9}$$

Magnetic field in z direction

$$H_{qwfRasB_z} = \frac{p_x^2}{2m} + \frac{1}{2}m\omega_x^2x^2 + \frac{\hbar^2k_y^2}{2m} + \frac{\hbar^2k_yk_{so}\sigma_x}{m} - \frac{\alpha}{\hbar}\sigma_yp_x + \frac{1}{2}g\mu_B\sigma_zB_z \tag{A.10}$$

Note: The eigenenergy expressions for the Hamiltonian representing the quantum wire in the full Rashba regime are too large and complicated to display.

Appendix B

Matrix representations of the Hamiltonians

This Appendix presents the matrix expressions of the Hamiltonians for the quantum wire for both Rashba regimes. Also given as an example are the eigenenergy levels obtained by the diagonalisation of the Hamiltonians for magnetic field applied in the transverse (x) direction for both zero and strong Rashba limits in the normal Rashba and for strong Rashba limit in the full Rashba regime.

B.1 Normal and full Rashba Hamiltonian matrix expressions

Normal Rashba Hamiltonian matrix:

$$H_{nRas} = \begin{pmatrix} A1 & -M & 0 & 0 & 0 & 0 & 0 & 0 \\ M & A2 & 0 & 0 & 0 & 0 & 0 & 0 \\ 0 & 0 & B1 & -M & 0 & 0 & 0 & 0 \\ 0 & 0 & M & B2 & 0 & 0 & 0 & 0 \\ 0 & 0 & 0 & 0 & C1 & -M & 0 & 0 \\ 0 & 0 & 0 & 0 & M & C2 & 0 & 0 \\ 0 & 0 & 0 & 0 & 0 & 0 & D1 & -M \\ 0 & 0 & 0 & 0 & 0 & 0 & M & D2 \end{pmatrix} \tag{B.1}$$

Full Rashba Hamiltonian matrix:

$$H_{fRas} = \begin{pmatrix} A1 & -M & 0 & \sqrt{2}\,\omega_{so} & 0 & 0 & 0 & 0 \\ M & A2 & -\sqrt{2}\,\omega_{so} & 0 & 0 & 0 & 0 & 0 \\ 0 & -\sqrt{2}\,\omega_{so} & B1 & -M & 0 & 2\,\omega_{so} & 0 & 0 \\ \sqrt{2}\,\omega_{so} & 0 & M & B2 & -2\,\omega_{so} & 0 & 0 & 0 \\ 0 & 0 & 0 & -2\,\omega_{so} & C1 & M & 0 & \sqrt{6}\,\omega_{so} \\ 0 & 0 & 2\,\omega_{so} & 0 & M & C2 & -\sqrt{6}\,\omega_{so} & 0 \\ 0 & 0 & 0 & 0 & 0 & -\sqrt{6}\,\omega_{so} & D1 & -M \\ 0 & 0 & 0 & 0 & \sqrt{6}\,\omega_{so} & 0 & M & D2 \end{pmatrix} \tag{B.2}$$

where

$$\begin{aligned} M &\equiv iB_y + B_z, \\ A1 &\equiv 1 + B_x + 2\,\omega_{so}\,\omega_y + {\omega_y}^2, \\ A2 &\equiv 1 - B_x - 2\,\omega_{so}\,\omega_y + {\omega_y}^2, \\ B1 &\equiv 3 + B_x + 2\,\omega_{so}\,\omega_y + {\omega_y}^2, \\ B2 &\equiv 3 - B_x - 2\,\omega_{so}\,\omega_y + {\omega_y}^2, \\ C1 &\equiv 5 + B_x + 2\,\omega_{so}\,\omega_y + {\omega_y}^2, \\ C2 &\equiv 5 - B_x - 2\,\omega_{so}\,\omega_y + {\omega_y}^2, \\ D1 &\equiv 7 + B_x + 2\,\omega_{so}\,\omega_y + {\omega_y}^2, \text{ and} \\ D2 &\equiv 7 - B_x - 2\,\omega_{so}\,\omega_y + {\omega_y}^2. \end{aligned}$$

Note: $k_{so}l_\omega \equiv \omega_{so}$, $k_y l_\omega \equiv \omega_y$ and $(k_y l_\omega)^2 \equiv {\omega_y}^2$

B.2 Examples of Hamiltonian matrix expressions and their eigenenergy levels

The Hamiltonian matrix expressions of the wire for magnetic field applied in the transverse (x) direction at zero and strong Rashba limits in the normal Rashba model and for the strong Rashba limit in the full Rashba model are given together with their respective eigenenergy levels (obtained via numerical diagonalisation).

Normal Rashba for zero Rss:

Setting $B_y = B_z = \omega_{so} = 0$ in Eq. B.1 yeilds the Hamiltonian matrix that describes the motion of electrons in the wire with external magnetic field applied in the x direction only and in the absence of spin–orbit interaction given by

$$H_{nRas,0} = \begin{pmatrix} E1 & 0 & 0 & 0 & 0 & 0 & 0 & 0 \\ 0 & E2 & 0 & 0 & 0 & 0 & 0 & 0 \\ 0 & 0 & F1 & 0 & 0 & 0 & 0 & 0 \\ 0 & 0 & 0 & F2 & 0 & 0 & 0 & 0 \\ 0 & 0 & 0 & 0 & G1 & 0 & 0 & 0 \\ 0 & 0 & 0 & 0 & 0 & G2 & 0 & 0 \\ 0 & 0 & 0 & 0 & 0 & 0 & H1 & 0 \\ 0 & 0 & 0 & 0 & 0 & 0 & 0 & H2 \end{pmatrix} \tag{B.3}$$

where

$$\begin{aligned} E1 &\equiv 1 + B_x + {\omega_y}^2, \\ E2 &\equiv 1 - B_x - {\omega_y}^2, \\ F1 &\equiv 3 + B_x + {\omega_y}^2, \\ F2 &\equiv 3 - B_x - {\omega_y}^2, \\ G1 &\equiv 5 + B_x + {\omega_y}^2, \\ G2 &\equiv 5 - B_x - {\omega_y}^2, \\ H1 &\equiv 7 + B_x + {\omega_y}^2, \text{ and} \\ H2 &\equiv 7 - B_x - {\omega_y}^2. \end{aligned}$$

Since the above matrix (Eq. B.3) is already in diagonal form the matrix elements $E1$ through $H2$ are the derived eigenenergy levels for the quantum wire in the absence of spin–orbit interaction and with field applied in the x direction. The matrix (Eq. B.3) is diagonal because the eigenenergy expression comprises of terms that share the same eigenstates (i.e., of σ_x) and represent shifted oscillator energy levels due to the terms H_{sb} (Eq. 2.22), H_{1D} (Eq. 2.23), and the x component of H_z (Eq. 2.24).

Normal Rashba for strong Rss:

For the strong Rss case that is when $\omega_{so} = 0.9$ the matrix expression Eq. B.1 becomes

$$H_{nRas,0.9} = \begin{pmatrix} I1 & 0 & 0 & 0 & 0 & 0 & 0 & 0 \\ 0 & I2 & 0 & 0 & 0 & 0 & 0 & 0 \\ 0 & 0 & J1 & 0 & 0 & 0 & 0 & 0 \\ 0 & 0 & 0 & J2 & 0 & 0 & 0 & 0 \\ 0 & 0 & 0 & 0 & K1 & 0 & 0 & 0 \\ 0 & 0 & 0 & 0 & 0 & K2 & 0 & 0 \\ 0 & 0 & 0 & 0 & 0 & 0 & L1 & 0 \\ 0 & 0 & 0 & 0 & 0 & 0 & 0 & L2 \end{pmatrix} \tag{B.4}$$

where

$$\begin{aligned}
I1 &\equiv 1 + B_x + 1.8\,\omega_y + {\omega_y}^2,\\
I2 &\equiv 1 - B_x - 1.8\,\omega_y + {\omega_y}^2,\\
J1 &\equiv 3 + B_x + 1.8\,\omega_y + {\omega_y}^2,\\
J2 &\equiv 3 - B_x - 1.8\,\omega_y + {\omega_y}^2,\\
K1 &\equiv 5 + B_x + 1.8\,\omega_y + {\omega_y}^2,\\
K2 &\equiv 5 - B_x - 1.8\,\omega_y + {\omega_y}^2,\\
L1 &\equiv 7 + B_x + 1.8\,\omega_y + {\omega_y}^2, \text{ and}\\
L2 &\equiv 7 - B_x - 1.8\,\omega_y + {\omega_y}^2
\end{aligned}$$

are the eigenenergy levels.

Full Rashba for strong Rss:

Setting $\omega_{so} = 0.9$ in Eq. B.2 yields the Hamiltonian

$$H_{fRas,0.9} = \begin{pmatrix}
A1 & 0 & 0 & 0.9\sqrt{2} & 0 & 0 & 0 & 0\\
0 & A2 & -0.9\sqrt{2} & 0 & 0 & 0 & 0 & 0\\
0 & -0.9\sqrt{2} & B1 & 0 & 0 & 1.8 & 0 & 0\\
0.9\sqrt{2} & 0 & 0 & B2 & -1.8 & 0 & 0 & 0\\
0 & 0 & 0 & -1.8 & C1 & 0 & 0 & 0.9\sqrt{6}\\
0 & 0 & 1.8 & 0 & 0 & C2 & -0.9\sqrt{6} & 0\\
0 & 0 & 0 & 0 & 0 & -0.9\sqrt{6} & D1 & 0\\
0 & 0 & 0 & 0 & 0.9\sqrt{6} & 0 & 0 & D2
\end{pmatrix}, \tag{B.5}$$

which can be diagonalised numerically to extract its eigenenergy levels. Since Eq. B.5 has off–diagonal matrix elements due to the inclusion of the H_{mix} (Eq. 2.18) term in the wire model, the eigenenergy levels are lengthy and complicated to display.

Appendix C

Typical physical parameters encountered in GaAs/AlGaAs heterostructures and their values

In this Appendix expressions of some physical parameters applied to GaAs/AlGaAs heterostructures are presented. These parameters are calculated using typical values for electron density and electron mobility as shown.

Electron density $n_s = 2.8 \times 10^{15}\,\mathrm{m}^{-2}$

Electron mobility $\mu_e = 10^6\,\mathrm{cm}^2\,\mathrm{V}^{-1}\,\mathrm{s}^{-1}$

Effective mass $m = 0.067 m_o$, where m_o is the rest mass of the electron

Scattering time $\tau = m\mu_e/e = 38\,\mathrm{ps}$, where e is the electronic charge

Fermi energy $E_F = \pi\hbar^2 n_s/m = 10\,\mathrm{meV}$

Fermi velocity $v_F = \sqrt{(2E_F/m)} = 2.3 \times 10^5\,\mathrm{m\,s}^{-1}$

Fermi wavelength $\lambda_F = \sqrt{(2\pi/n_s)} = 47\,\mathrm{nm}$

Elastic mean free path $\ell_e = v_F\tau = 8.7\,\mu\mathrm{m}$

Magnetic length $l_B = \sqrt{\hbar/eB} = 8.1\,\mathrm{nm}$ at $B = 10\,\mathrm{T}$

Effective g factor $g^* = 0.14$

Note: Data adapted from Mesoscopic Electron Transport (Kluwer Academic Publishers, 1997) [18].

Bibliography

[1] B. Kramer, K. Dittmer, S. Debald, J. Ohe, F. Cavaliere and M. Sassetti, Spin transport through nanostructures, Materials Science–Poland **22**, No. 4, 445 (2004).

[2] D.D. Awschalom, N. Samarth, and D. Loss, Eds., Semiconductor Spintronics and Quantum Computation, (Springer, Berlin, 2002).

[3] S.A. Wolf, D.D. Awschalom, R.A. Buhrmann, J.M. Daughton, S. von Molnar, M.L. Roukes, A.Y. Chtchelkanova, D.M. Treger, Spintronics: A Spin–based electronics vision for the future, Science **294**, 1488 (2001).

[4] S. Datta and B. Das, Electronic analog of the electro–optic modulator, Appl. Phys. Lett. **56**, 665 (1990).

[5] H.-Q. Zhou and S.Y. Cho, Spin–charge conductance in nanoscale electronic devices, J. Phys: Condens. Matter **17**, 7433 (2005).

[6] G.A. Prinz, Spin–polarized electron transport, Phys. Today **48**, No. 4, 58 (1995); G.A. Prinz, Magnetoelectronics, Science **282**, 1660 (1998).

[7] A. Brataas, Y.V. Nazarov and G.E.W. Bauer, Finite–element theory of transport in ferromagnetnormal metal systems, Phys. Rev. Lett. **84**, No. 11, 2481 (2000).

[8] K. Inomata, Giant magnetoresistance and its sensor applications, J. Electroceramics **2**, No. 4, 283 (1998).

[9] C. Weisbuch and B. Vinter, Quantum Semiconductor Structures: Fundamentals and Applications, (Elsevier, 1991).

[10] S. Datta, Electronic Transport in Mesoscopic Systems, (Cambridge University Press, 1995).

[11] D.K. Ferry and S.M. Goodnick, Transport in Nanostructures, (Cambridge University Press, 1997).

[12] H. van Houten and C. Beenakker, Quantum point contacts, Phys. Today **49**, Issue 7, 22 (1996).

[13] K. von Klitzing, The Quantized Hall effect, Rev. Mod. Phys. **58**, 519 (1986).

[14] R.B. Laughlin, Nobel Lecture: Fractional Quantization, Rev. Mod. Phys. **71**, 863 (1998).

[15] H.L. Stormer, Nobel Lecture: The Fractional Quantum Hall Effect, Rev. Mod. Phys. **71**, 875 (1998).

[16] H.L. Stormer, D.C. Tsui, and A.C. Gossard, The Fractional Quantum Hall effect, Rev. Mod. Phys. **71**, S298 (1999).

[17] D.C. Tsui, Nobel Lecture: Interplay of Disorder and Interaction in Two–Dimensional Electron Gases in Intense Magnetic Fields, Rev. Mod. Phys. **71**, 891 (1998).

[18] L.L. Sohn, L.P. Kouwenhoven and G. Schön, Eds., Mesoscopic Electron Transport, (Kluwer Academic Publishers, 1997).

[19] P. Havu, M.J. Puska and R.M. Nieminen, Electron transport through ballistic quantum wires and point contacts, Phys. Rev. B **70**, 233308 (2004).

[20] C.W.J. Beenakker and H. van Houten, Quantum transport in semiconductor nanostructures, Solid State Phys. **44**, 1 (1991).

[21] B.L. Altshuler, P.A. Lee, and R.A. Webb, Eds., Mesoscopic Phenomena in Solids, North Holland, Amsterdam (1991).

[22] E. Akkermans, G. Montambaux, J.-L. Pichard, and J. Zinn-Justin, Eds., Mesoscopic Quantum Physics, North Holland, Amsterdam (1995).

[23] T. Heinzel, Mesoscopic Electronics in Solid State Nanostructures, (Wiley-VCH, 2003).

[24] Y. Imry, Introduction to Mesoscopic Physics: Mesoscopic Physics and Nanotechnology, (Oxford University Press, 1997).

[25] P.L. Taylor and O. Heinonen, A Quantum Approach to Condensed Matter Physics, (Cambridge University Press, 2002).

[26] L. Serra, D. Sánchez and R. López, Rashba interaction in quantum wires with in–plane magnetic fields, Phys. Rev. B **72**, 235309 (2005).

[27] E.I. Rashba, Fiz Tverd. Tela (Leningrad) 2, 1224 (1960) [Sov. Phys. Solid State 2, 1109 (1960)]; Y.A. Bychkov an E.I. Rashba, Oscillatory effects and magnetic susceptibility of carriers in inversion layers, J. Phys. C: Solid State **17**, 6039 (1984); Y.A. Bychkov an E.I. Rashba, Properties of 2D electron gas with lifted spectral degeneracy, JETP Lett. **39**, No. 2, 78 (1984).

[28] E.I. Rashba, Electron spin operation by electric fields: spin dynamics and spin injection, Physica E. **20**, 189 (2004).

[29] E.I. Rashba, Spin–orbit coupling and spin transport, Physica E. **34**, 31 (2006).

[30] M.Valín-Rodríguez, A. Puente and L. Serra, Electron spin precession in semiconductor quantum wires with Rashba spin–orbit coupling, Eur. Phys. J. B **34**, 359 (2003).

[31] J.P. Heida, B.J. van Wees, J.J. Kuipers and T.M. Klapwijk, Spin–orbit interaction in a two–dimensional electron gas in a InAs/AlSb quantum well with gate–controlled electron density, Phys. Rev. B **57**, 11911 (1998).

[32] L.W. Molenkamp, G. Schmidt and G.E.W. Bauer, Rashba Hamiltonian and electron transport, Phys. Rev. B. **64**, 121202(R) (2001).

[33] J. Nitta, T. Akazaki, H. Takayanagi and T. Enoki, Gate control of spin–orbit interaction in an inverted $In_{0.53}Ga_{0.47}AsIn_{0.52}Al_{0.48}As$ heterostructure, Phys. Rev. Lett. **78**, 1335 (1997).

[34] D. Grundler, Large Rashba splitting in InAs quantum wells due to electron wave function penetration into the barrier layers, Phys. Rev. Lett. **84**, 6074 (2000).

[35] T. Matsuyama, R. Kürsten, C. Meiner and U. Merkt, Rashba spin splitting in inversion layers on p–type bulk InAs, Phys. Rev. B. **61**, 15588 (2000).

[36] T. Ando and H. Tamura, Conductance fluctuations in quantum wires with spin–orbit and boundary–roughness scattering, Phys. Rev. B **46**, 2332 (1992).

[37] A.V. Moroz and C.H.W. Barnes, Effect of the spin–orbit interaction on the band structure and conductance of quasi–one–dimensional systems, Phys. Rev. B **60**, No. 20, 14272 (1999).

[38] M. Governale and U. Zülicke, Spin accumulation in quantum wire with strong Rashba spin–orbit coupling Phys. Rev. B **66**, 073311 (2002).

[39] M. Governale and U. Zülicke, Rashba spin splitting in quantum wires, Solid State Comm. **131**, 581 (2004).

[40] K.-F. Berggren, T.J. Thornton, D.J. Newson and M. Pepper, Magnetic depopulation of 1D subbands in a narrow 2D electron gas in a GaAs:AlGaAs heterojunction, Phys. Rev. Lett. **57**, No. 14, 1769 (1986).

[41] K.-F. Berggren, G. Roos and H. van Houten, Characterization of very narrow quasi–one–dimensional quantum channels, Phys. Rev. B. **37**, No. 17, 10118 (1988).

[42] H.L. Zhao, Y. Zhu and S. Feng, Magnetic depopulation of hybrid magnetoelectric subbands in a quantum–well wire under an axial magnetic field, Phys. Rev. B. **40**, No. 11, 8107 (1989).

[43] A.V. Moroz and C.H.W. Barnes, Spin–orbit interaction as a source of spectral and transport properties in quasi–one–dimensional systems, Phys. Rev. B **61**, R2464 (2000).

[44] P. Středa and P. Šeba, Antisymmetric spin filtering in one–dimensional electron systems with uniform spin–orbit coupling, Phys. Rev. Lett. **90**, 256601 (2003).

[45] Y.V. Pershin, J.A. Nesteroff and V. Privman, Effect of spin–orbit interaction and in–plane magnetic field on the conductance of a quasi–one–dimensional system, Phys. Rev. B **69**, 121306(R) (2004).

[46] R.G. Pereira and E. Miranda, Magnetically controlled impurities in quantum wires with strong Rashba coupling, Phys. Rev. B **71**, 035311 (2005).

[47] S. Debald and B. Kramer, Rashba effect and magnetic field in semiconductor quantum wires, Phys. Rev. B **71**, 115322 (2005).

[48] M. Zarea and S.E. Ulloa, Landau level mixing by full spin–orbit interactions, Phys. Rev. B **72**, 085342 (2005).

[49] G. Dresselhaus, Spin–orbit coupling effects in zinc blende structures, Phys. Rev. **100**, 580 (1955).

[50] F. Mireles and G. Kirczenow, Ballistic spin–polarized transport and Rashba spin precession in semiconductor nanowires, Phys. Rev. B **64**, 024426 (2001).

[51] R. Shankar, Principles of Quantum Mechanics 2nd edition, (Plenum Press, New York, 1980).

[52] S. Gasiorowicz, Quantum Physics 3rd edition, (John Wiley & Sons Inc., 2003).

[53] J.H Davies, The Physics of Low–Dimensional Semiconductors: An Introduction, (Cambridge University Press, 1998).

[54] S. Blügel, M. Luysberg, K. Urban and R. Waser, Eds., Lecture manuscripts of the 34th Spring School of the Department of Solid State Research: Fundamentals of Nanoelectronics, (Forschungszentrum Jülich, 2003).

[55] J. Knobbe and Th. Schäpers, Magnetosubbands of semiconductor quantum wires with Rashba spin–orbit coupling, Phys. Rev. B **71**, 035311 (2005).

[56] E. Emberly and G. Kirczenow, Electrical conductance of molecular wires, Nanotechnology **10**, 285 (1999).

[57] H. Mehrez, A. Wlasenko, B. Larade, J. Taylor, P. Grütter and H. Guo, I–V characteristics and differential conductance fluctuations of Au nanowires, Phy. Rev. B **65**, 195419 (2002).